This is a preprint, the final version is subject to change, of the American Mineralogist (MSA)
Cite as Authors (Year) Title. American Mineralogist, in press.
DOI: https://doi.org/10.2138/am-2018-6195

REVISION 001 – January 2018

Visible and short wave infrared reflectance spectroscopy of selected REE-bearing silicate minerals

DAVID J. TURNER[1,*], BENOIT RIVARD[2], LEE A. GROAT[1]

[1]Department of Earth, Ocean and Atmospheric Sciences, University of British Columbia, Vancouver, British Columbia V6T 1Z4, Canada

[2] Department of Earth and Atmospheric Sciences, University of Alberta, Edmonton, Alberta T6G 2E3. Canada

*E-mail: dturner@eos.ubc.ca

ABSTRACT

Natural samples of the rare earth element (REE)-bearing silicate minerals cerite, mosandrite, kainosite, zircon, and eudialyte were studied using reflectance spectroscopy in the visible to short-wave infrared regions (500 to 2500 nm) and further characterized by scanning electron microscopy and electron microprobe analysis. Spectral features of these minerals are driven primarily by 4*f*-4*f* intraconfigurational electronic transitions of trivalent lanthanides, as well as 5*f*-5*f* electronic transitions of uranium and vibrational overtones and combinations of H_2O and OH^-. Spectra of eudialyte are also impacted by relative amounts of $^{IV}Fe^{2+}$ and $^{V}Fe^{2+}$. Respective spectra of these REE-bearing silicate minerals are sufficiently distinct to enable spectral classification. Spectral variability (e.g., band depths and locations) of some specific REE-related absorptions, such as an Er^{3+}- and Yb^{3+}-related absorption near 978 nm and Nd^{3+}-related absorptions near 746, 803, and 875 nm, are interpreted to be driven by cation site

differences in the crystal structures. This work adds to the growing understanding of REE-bearing mineral reflectance spectroscopy, which facilitates detection, identification, and quantification of REE-bearing silicate minerals in remote sensing applications. This is especially relevant for hyperspectral imaging spectroscopy with high spatial resolutions where the spectral response of a pixel becomes increasingly dominated by mineralogy rather than lithology.

INTRODUCTION

Reflectance spectroscopy is being applied to a growing number of fields within the geosciences and at the same time there has been renewed interest in rare earth element deposits and minerals. Fundamental research at the intersection of these fields has been lacking, and here we provide detailed reflectance spectroscopy on several important rare earth element bearing silicate minerals. These minerals show a large diversity of overall crystal structures, chemical compositions, and host sites for the lanthanides. They can show strong enrichment in light rare earth elements (LREE, e.g., cerite), heavy rare earth elements (HREE, e.g., kainosite), or display relatively elevated values of all REE (e.g., mosandrite). The REE can form specific structural components (e.g., kainosite), be important constituents across multiple sites (e.g., eudialyte), or exist as trace to minor elements (e.g., zircon). The suite of minerals studied here (cerite, mosandrite, kainosite, zircon, and eudialyte) covers a wide breadth of variability but is by no means entirely comprehensive.

The REE-bearing silicate minerals can be locally abundant and contain high amounts of REE but have been traditionally viewed negatively with respect to their economic significance as compared to the REE phosphates and fluorocarbonates. Recent mineral exploration and metallurgical developments, however, are proving that some silicate phases are amenable to beneficiation (e.g., Mariano and Mariano 2012). Understanding differences in the spectral

responses of REE-bearing silicates is important if reflectance spectroscopy is to be used in the exploration and exploitation of these commodities. The use of REE-bearing silicate minerals as geochronometers, especially zircon, provides an additional motivation for understanding the spectral responses of these minerals. Hancock et al. (2012) suggested that recognizing spectra of zircon in large spectral databases, such as hyperspectral core logs, could facilitate petrological studies by identifying areas with suitable (i.e., non-metamict) zircon.

This research builds on studies by Turner et al. (2014, 2016) that document the reflectance spectra of REE-bearing fluorocarbonate and phosphate minerals. Those publications documented that the strength of absorption features due to the lanthanides will primarily be a function of the concentration of the ion and the location of the absorption features will be primarily a function of the cation's specific coordination and asymmetry in the host crystal structure. The presentation of the results of this study is similarly structured and intended to form a body of reference literature for the spectral characteristics of REE bearing minerals. The mineralogical and spectroscopic background of REE-bearing minerals is provided, followed by band registries and interpretations of spectral absorption features.

REVIEW OF REFLECTANCE SPECTROSCOPY STUDIES OF REE-BEARING SILICATE MINERALS

The widely used USGS spectral library (Version 06, Clark et al. 2007) contains one spectrum for zircon from Brazil and one spectrum for metamict allanite from Ontario. Version 2 of the ASTER Library (Baldridge et al. 2009) contains one spectrum of zircon from Malawi. No chemical data are available for these samples. Kerr et al. (2011) presented five excellent spectra of eudialyte from the Red Wine Intrusive Suite that show evidence of Ln^{3+} absorption bands but they provided no chemical data or interpretation of the spectra. Neave et al. (2016) studied

reflectance spectra from a range of mostly REE-bearing carbonatite rocks, but included one hand sample with eudialyte from Illimausaq whose mean spectrum (n = 73) shows subtle REE-related absorptions at ~744 and ~802 nm. Hancock et al. (2012) reported on the potential of reflectance spectroscopy to identify zircon in drill core and hand samples using U-related absorptions. Abstracts by Swayze et al. (2013) and Hoefen et al. (2013) showed that baseline and applied research is being conducted on REE minerals and deposits by the USGS.

Thus, there remains an information gap for the interpretation of reflectance spectra from REE-bearing silicates, with respect to identifying and explaining spectral features as well as in supporting the discrimination of minerals based on their spectral characteristics. Nevertheless, the optical and infrared spectroscopy of zircon and eudialyte have been studied in detail and reviews are warranted to understand factors that affect their reflectance spectra, especially where they overlap with Ln^{3+}-related features.

Spectroscopy of zircon

Richman et al. (1967) and Fielding (1970) provided early studies of the absorption spectrum of zircon in the visible and infrared, which have been followed by a variety of techniques due to zircon's importance for geochronology and its potential as a storage phase for nuclear waste, among many other applications. Zircon has been shown to incorporate significant amounts of both uranium and lanthanides in a variety of oxidation states.

With respect to uranium in zircon, Vance and Mackey (1978) established energy levels for U^{4+} and U^{5+} in zircon, hafnon, and thorite. Their strongest absorption bands for U^{4+} were located at 1682, 1119, 653, 636, and 537 nm. They also observed the U^{5+} absorption bands at 1107 and 1492 nm. Krupa and Carnall (1993) studied the energy levels of U in $ThSiO_4$ in greater detail,

providing a more thorough evaluation of specific levels but in a different host lattice. Kempe et al. (2010) investigated a suite of zircon samples using a variety of spectroscopic techniques, including optical absorption. Their sample from Mt. Malosa, which was notably reported to be metamict, showed a few bands in the VIS range (up to ~900 nm) that they related to Nd^{3+} and Er^{3+}. Kempe et al. (2010) also found evidence for minor amounts of U^{6+} in zircon in the form of uranyl (UO_2^{2+}) through the use of time-resolved laser-induced photoluminescence. Zhang et al. (2002, 2003) used infrared absorption spectroscopy to study select features related to Si-O, OH, U^{4+}, and U^{5+} in zircon. Notably, they observed that: (1) U^{5+} at a crystalline site shows absorption at 6668 cm^{-1} (1500 nm) and with continued radiation damage is replaced by (not shifted to) U^{5+} at an amorphous site with absorption at 6650 cm^{-1} (1504 nm); (2) U^{5+} at a crystalline site shows absorption at 9030 cm^{-1} (1107 nm) and with continued radiation damage is replaced by (not shifted to) U^{5+} at an amorphous site with absorption at 8969 cm^{-1} (1115 nm); (3) U^{4+} at a crystalline site shows absorption at 4833 cm^{-1} (2069 nm), which broadens with radiation damage, and the location of maximum absorption shifts towards 4800 cm^{-1} (2083 nm); and (4) other prominent U^{4+} crystalline absorption bands were reported at 10922 (916 nm), 6779 (1475 nm), 6508 (1537 nm), 6022 (1661 nm), 5861 (1706 nm), and 4567 cm^{-1} (2190 nm).

With respect to lanthanides in zircon, ligand-metal charge transfer bands, interelectronic charge transfers and lanthanide-dependant electron holes have all been documented. Hansen *et al.* (1996) describe a 4*f*-5*d* transition for Tb^{4+} in zircon in the UV range near 280 nm. Similarly, Kempe et al. (2010) concluded that charge-transfer bands for Pr^{4+} and perhaps Tb^{4+} in the UV show tails that extend into the VIS range, impacting color as in synthetic Pr-bearing zircon yellow pigments (e.g., Badenes et al. 2002). Klinger et al. (2012) investigated the role that electron holes and crystal defects play in generating color in zircon. Their crystals ranged from

colorless through yellow-brown to red and they identified two principal electron hole-related bands that are centered at ~340-350 and ~510-515 nm with full-width at half-maximum (FWHM) values of ~175 nm. These electron holes were found to be dependent on the existence of lanthanides in zircon. Simlarly, Laruhin et al. (2002) reported the conversion of Dy^{3+} to Dy^{4+} and of Tb^{3+} to Tb^{4+} from incident radiation, however, it was unclear as to what proportion of the Dy and Tb was being converted during their laboratory experiments and what could be expected in nature.

The ability of zircon to host various cations in various oxidation states and to display a multitude of defect centers makes the details of optical spectroscopy difficult to unravel, however, the majority of the spectroscopic impact and subsequent research is within the UV and VIS ranges.

Spectroscopy of eudialyte

Eudialyte has been well studied because of its striking pink-red color and challenging crystal structure and variable crystal chemistry. Polshin et al. (1991), Burns (1996), and Rossman and Taran (2001) discussed the four- and five-fold coordination of Fe^{2+} in eudialyte at the M2 site. In four-fold coordination, $^{IV}Fe^{2+}$ assumes a square-planar arrangement with O^{2-} that leads to absorptions centered near 529 nm (18900 cm^{-1}) and 1366 nm (7320 cm^{-1}). In five-fold coordination, $^{V}Fe^{2+}$ assumes a pyramidal arrangement with four O^{2-} and one OH^{-} at the apex of the pyramid, leading to absorptions centered near 917 nm (10900 cm^{-1}) and 2500 nm (4000 cm^{-1}). The result is that eudialyte with predominantly $^{IV}Fe^{2+}$ shows pink to crimson-red colors whereas eudialyte with $^{V}Fe^{2+}$ has brownish hues. These yellow-brown or red-brown varieties are also known by the unofficial name *eucolite*. Eudialyte is also host to Fe^{3+} but typically in lesser amounts. Manganese in eudialyte is assumed to be divalent and in either five-fold (M2 site) or

six-fold (M1 site) coordination, according to Johnsen et al. (1998, 2001). Burns (1996) lists five main bands for Mn^{2+}, located near 535, 440, 405, 355, and 345 nm depending on the mineral host. No systematic studies of REE-related spectroscopy have been carried out on eudialyte that the authors are aware of.

CRYSTAL STRUCTURE REVIEWS

The REE-bearing silicate minerals show a wide range of coordinations and overall crystal chemistry and structure. Coordination numbers range from six (gittinsite) to 11 (allanite), with some cases showing 8+1 coordination (cerite) and other minerals having more than one distinct REE site (mosandrite). Documented bond lengths vary accordingly, ranging from ~2.2 to ~3.2 Å. Understanding the differences in crystal structures provides context for how the lanthanide-related absorption bands vary (Table 1).

Cerite-(Ce), ideally $Ce_9Fe^{3+}(SiO_4)_6(SiO_3OH)(OH,F)$, contains three distinct but similar REE sites that are all nine-coordinated with average bond lengths of ~2.59 Å, but individual bond lengths vary from 2.41 to 3.00 Å (Moore and Shen 1983, Pakhomovsky et al. 2002). Each of these three sites is bonded to eight oxygen atoms and an (OH,F) group with REE-OH distances of 2.55, 2.59, and 2.49 Å (Fig. 1). Total REO is ~ 73% and although cerite has not been identified at many localities, it is present in significant volumes at type locations such as Bastnas (Vastmanland, Sweden) and the Mountain Pass mine (California, USA).

Mosandrite is a complex titanium silicate with REO contents of up to ~25% that has been studied in detail by Sokolova and Camara (2008) and Bellezza et al. (2009), but with slightly different outcomes. According to Sokolova and Camara (2008) the ideal formula is $Na_2Ca_4REETi(Si_2O_7)_2OF_3$. Using their refinement, REE in mosandrite occupy two seven-

158 coordinated sites with bond lengths from 2.403 to 2.674 Å (A^P site, average = 2.484 Å) and
159 2.353 to 2.749 Å (M^H site, average = 2.452 Å). The A^P site is coordinated to six oxygen and a
160 single F atom whereas the M^H site is coordinated by six oxygen atoms and a mixed-occupancy
161 anion site. Bellezza et al. (2009) gave a more flexible formula of
162 $Ti(□,Ca,Na)_3(Ca,REE)_4(Si_2O_7)_2[H_2O,OH,F]_4*1H_2O$, which notably includes structural H_2O.
163 Refinements suggest REE primarily at the very similar seven-coordinated M4 and M5 sites,
164 which are comparable to the two described by Sokolova and Camara (2008), as well as allowing
165 small amounts of REE (~10% of total REE content) at a third six-coordinated site (M3) with
166 slightly shorter bond lengths (Fig. 1). This M3 site is bonded to atoms at two oxygen and four
167 mixed anion sites. The mixed anion site OF(1) is also coordinated to the M1 site, which hosts
168 Ti^{4+}. Our spectrum for mosandrite favors the H_2O-bearing structure suggested by Bellezza et al.
169 (2009).

170 Kainosite-(Y), ideally $Ca_2Y_2(SiO_3)_4(CO_3)\cdot H_2O$, is typically found in alkalic pegmatites
171 and contains up to ~40% REO with a strong preference for yttrium and the HREE. The REE
172 occur at a single fairly symmetric site with eight-fold coordination and bond lengths between
173 2.24 and 2.52 Å (Fig. 1). Kainosite is host to CO_3 with an average C-O bond length of 1.2526 Å,
174 but it is asymmetric because two of the three edges of the CO_3 plane share edges with adjacent
175 YO_8 polyhedra (Rumanova et al. 1967).

176 Zircon, $ZrSiO_4$, although not an "REE mineral", is a common carrier of moderate amounts of
177 REE (e.g., Sheard et al. 2012), along with Th, U, Hf, and other high field-strength elements
178 (HFSE). Collectively, the articles by Finch et al. (2001), Hanchar et al. (2001), and Finch and
179 Hanchar (2003) cover the incorporation of REE into zircon in great detail. Synthetic REE-doped
180 zircon showed the coupled xenotime-substitution "$REE^{3+} + P^{5+} = Zr^{4+} + Si^{4+}$," whereby REE

enter the fairly symmetric eight-coordinated Zr site (Fig. 1) and are charge-balanced by P^{5+} replacing Si^{4+}. Bond lengths for (Zr,REE)-O range from 2.130 to 2.278 Å, and total REO content usually only attains ~5% with a preference for HREE + Y. Friis et al. (2010) studied the photoluminescence of REE-doped zircon from ~250 to 600 nm and among their conclusions they showed that REE in zircon is hosted in two ZrO_8 polyhedra that are slightly non-equivalent. Finch and Hanchar (2003) also noted that interstitial sites are a possibility for hosting smaller high field-strength elements.

The eudialyte group comprises at least 25 approved mineral species and the crystal chemistry of the group allows for up to ~10% REO (Johnsen and Grice 1999, Johnsen et al. 2003). The minerals of this group are Na-rich zirconosilicates with three- and nine-membered rings of SiO_4. The general formula of the mineral group is: $Na_{15}[M(l)]_6[M(2)]_3Zr_3[M(3)](Si_{25}O_{73})(O,OH,H_2O)_3X_2$, while eudialyte itself is $Na_{15}Ca_6(Fe^{2+},Mn^{2+})_3Zr_3Si[Si_{25}O_{73}](O,OH,H_2O)_3(OH,Cl)_2$. The REE typically occupy the M1 site (REE-O ~2.30 Å) in place of Ca with distorted six-fold coordination, as well as within the cavity-like Na(3) and Na(4) sites. The cavernous nature of the Na sites, however, forces the cations to occupy whatever space results from the various substitutions in this flexible formula. Johnsen and Grice (1999) noted that coordination of the Na sites can range from six to 10 and anions include oxygen and the contents of the X site, although the Na(4) position typically has a distorted nine-fold coordination polyhedron. Polyhedra in Figure 1 show the Na(4) site with possible oxygen atoms (red) and a mixed anion site (green). This figure (modified from Johnsen and Grice 1999) also shows the linkages to Si tetrahedra (magenta), the M2 site (grey polyhedra), and the M3 site (blue octahedra).

With respect to site assignment of REE in eudialyte-group minerals when only chemical data is available, Johnsen et al. (2001) and Johnsen and Grice (1999) recommended that all Ca be assigned to the M(1) site, and remaining space filled with Mn and subsequently REE. Remaining REE is assigned to the Na(4) site. With respect to the objectives of this work, it is likely that high-Ca samples will encourage REE to predominantly occupy the Na(4) site over the M(1) site. However, single-crystal refinements show that nearly all the compositions in Johnsen and Grice (1999) have REE at both sites, irrespective of Ca content. Consequently, this is likely the case when interpreting absorptions due to REE^{3+}.

EXPERIMENTAL METHODS

Samples

One cerite, one mosandrite, one kainosite, five zircon, and nine eudialyte samples without significant compositional zoning (as assessed via SEM) were selected from a larger suite as being suitable for this study. The zircon crystals originate from Green River (several crystals up to 0.5 cm long), Mudtank (crystal ~ 2 cm long), North Burgess (crystal ~1.5 cm long), Mt Malosa (rock with abundant clusters of small crystals ~1 mm long each), and St. Peters Dome (single crystal 0.75 cm across in hand sample). The kainosite specimen was three small patches (~3 × 3 mm) on a small hand sample. Cerite was found in dark pink-brown to grey massive aggregates within a ~10 × 10 cm hand sample. Hand sample F92-23 from Kipawa contained numerous crystals of both green-brown mosandrite (up to ~3 cm long, 0.5 cm wide) and patches of pink to red eudialyte up to ~2 × 1 cm. Two other samples of eudialyte from Kipawa, "Mariano Suite" and "UofA" were coarse monomineralic hand samples up to 5 cm across. The remaining six eudialyte samples all originate from Mont Saint-Hilaire (MSH) and comprise either euhedral single crystals or coarse polycrystalline aggregates from ~1 × 1 cm to ~3 × 3 cm in size. Of

these, CMNOC476 and 2045 are red in hue while the rest are brown to brick red. Reagent-grade lanthanide oxide powders, REE-doped Spectralon, and other REE mineral phases with EMPA data were also investigated in order to aid in band assignment.

Scanning electron microscopy and electron microprobe analysis

The Philips XL30 scanning electron microscope (SEM) at the University of British Columbia, which is equipped with an energy-dispersion X-ray spectrometer (EDS), was used for preliminary examination of mineral mounts of selected minerals and rock fragments studied by reflectance spectroscopy.

Unzoned samples were then analyzed by electron microprobe at the Saskatchewan Research Council's Advanced Microanalysis Centre using a Cameca SX-100 equipped with five tunable wavelength-dispersive spectrometers. Operating conditions were: 40° takeoff angle, beam energy of 15 keV, beam current of 20 nA, beam diameter of 5 μm. The MAN background intensity data were calibrated and continuum absorption corrected. Elements were acquired using analyzing crystals LLIF for Fe*K*α, Ta*L*α, Pr*L*α, Eu*L*α, Dy*L*α, Tm*L*α, Mn*K*α, La*L*α, Nd*L*α, Gd*L*α, Ho*L*α, Yb*L*α, Ba*L*α, Ce*L*α, Sm*L*α, Tb*L*α, Er*L*α, and Lu*L*α; PET for Ca*K*α, K*K*α, Cl*K*α, Ti*K*α, Nb*L*α, Y*L*α, Sr*L*α, Zr*L*α, P*K*α, U*M*α, and Th*M*α; and LTAP for Mg*K*α, F*K*α, Na*K*α, Si*K*α, and Al*K*α. Counting times were 10 s for Zr and P and 15 s for all other elements, with off-peak count times of 10 s. The standards (with elements) were SPI-barite (Ba), SPI-celestite (Sr), SPI-YAG (Y, Al), Smithsonian Cr-augite (Mg, Ca), Smithsonian ilmenite (Fe, Ti), Smithsonian apatite (F, P), Smithsonian microcline (K), Smithsonian zircon (Zr), Harvard albite (Si, Na), Cameca Mn (Mn), SPI2-TlCl (Cl), SPI2-Nb (Nb), SPI2-La (La), SPI2-Ce (Ce), SPI2-Pr (Pr), SPI2-Nd (Nd), SPI2-Sm (Sm), SPI2-Eu (Eu), SPI2-Gd (Gd), SPI2-Tb (Tb), SPI2-Dy (Dy), SPI2-Ho (Ho), SPI2-

Er (Er), SPI2-Tm (Tm), SPI2-Yb (Yb), SPI2-Lu (Lu), SPI2-Ta (Ta), SPI2-Th (Th), and SPI2-U (U). Formula calculations for each mineral are given in their respective sections.

Reflectance spectroscopy

Reflectance spectroscopy was primarily carried out using the sisuROCK instrumentation (manufactured by SPECIM Spectral Imaging Ltd.) at the University of Alberta's CoreSensing Facility, and data were handled with ENVI 4.4, a widely used and commercially available software package. Two imaging spectrometers ("cameras") acquired reflectance spectra in the visible-near infrared (VNIR, 396 to 1003 nm over 784 channels, for an average spectral resolution of 0.77 nm) and short-wave infrared (SWIR, 928 to 2530 nm over 256 channels, for an average spectral resolution of 6.26 nm) portions of the electromagnetic spectrum. Spatial resolution of the cameras was approximately 0.079 mm/pixel in the VNIR and 0.241 mm/pixel in the SWIR. Noise was very prevalent in the shortest wavelength portion of the VNIR camera below ~550 nm and moderate from 550 to ~650 nm. Averaging ~16 pixels resulted in reliable spectra in the noisier ranges that would be useable in spectral libraries. Samples were placed on a matte black surface that translates the samples under the camera and has very low reflectance across the sampled wavelength range. Some samples were propped up with foam blocks to ensure surfaces of interest faced the spectrometers and were in focus. All samples were thick enough to ensure that the reflectance spectra are representative of the mineral target. Reflectance spectra did not have the continuum removed so as to present the data unmodified and to facilitate comparison against other earlier studies.

Spectra presented originate from single crystals, multiple crystals within a single rock sample, and from multiple loose single crystals (Table 2). For single crystal samples or those with large grain sizes, simple Regions Of Interest (ROI) were used to select target pixels for

averaging. Samples of kainosite from Long Lake and zircon from Mt Malosa comprised smaller crystals on larger hand samples. For these two samples, a priori knowledge allowed several purer pixels of the target mineral to be located. In the VNIR imagery, the depth of distinct absorptions related to REE content (near 745 nm and 808 nm) were used for thresholding to obtain 'end member' pixels for averaging. In the SWIR imagery, these located spectra were averaged and used as an input spectrum for the Spectral Angle Mapper (SAM) algorithm (Kruse et al. 1993) to re-evaluate the entire scene. Strict thresholds on SAM output rule images (goodness-of-fit to the input spectrum) allowed discrete selections of pure 'end member' pixels that were averaged to generate a single representative spectrum.

For example, in the SWIR imagery for the Mt. Malosa zircon sample a single end-member pixel with a strong absorption at 1250 nm was chosen to perform spectral angle mapping (Figs. 2 and 3). A strict threshold of 0.02 was chosen and applied to the scene (51,490 pixels in total) to generate an ROI comprising only 40 pixels. The intent is to isolate only as many pixels as needed to extract a representative, low-noise, average spectrum from the target mineral without introducing signals from other minerals/materials. Too loose of a threshold inevitably includes non-representative pixels and discrete absorption features become subdued (e.g., absorption at 1389 nm). Figure 2 illustrates how sequentially less-strict thresholds (most strict @ 0.02 to least strict @ 0.1) result in sequentially larger ROIs, and Figure 3 illustrates how averaging spectra from different ROIs impacts the resulting average spectrum from this scene.

The position and shape of the absorption features were recorded using reflectance spectra (i.e., not continuum-removed spectra). Descriptors for absorption bands include MIN (minimum) with modifiers –st (strong), -w (weak), -n (noisy), and –b (broad), and SH (shoulders) with modifiers –w (weak) and –n (noisy). Noisy modifiers are typically restricted to the short and long

294 wavelengths of the VNIR spectrometer (<600 nm, >950 nm). Noisy and weak absorption bands
295 are typically restricted to scenarios where other spectra show reliable features near the same
296 wavelength position. For example, the ~627 nm noisy shoulder of LREE-enriched cerite was
297 confidently included based on the presence of a 625 nm absorption in LREE-enriched
298 bastnaesite.

299

300 ## ELECTRON MICROPROBE COMPOSITIONS

301

302 ### Cerite, Mosandrite and Kainosite

303 These three samples all show satisfactory totals (Appendix A) and have a range of LREE
304 and HREE contents. Formula contents for cerite were calculated based on 31 anions and are
305 consistent with the site occupancies reported by Moore and Shen (1983) and Pakhomovsky et al.
306 (2002). Formula contents for mosandrite were calculated based on four Si apfu, and are
307 consistent with the occupancies in Bellezza et al. (2009), including the presence of structural
308 H_2O and OH^-. Formula contents for kainosite were calculated based on 16 anions and are
309 consistent with the site occupancies reported by Rumanova et al. (1967).

310 ### Zircon

311 The five zircon samples studied all have satisfactory totals, although the St. Peters Dome
312 and Mt. Malosa samples are marginal, and they show a good diversity of chemical variation to
313 investigate their reflectance characteristics (Appendix B). The Mudtank sample shows no
314 detectable U and the lowest REE content of all samples. The St. Peters Dome sample has U

315 below detection and a slight enrichment in HREE, notably with Er_2O_3 and Yb_2O_3. The Mt.
316 Malosa samples show U below detection but the highest REE (TREO of 4.83 wt%). The North
317 Burgess sample contains moderate UO_2 and very low REE values. The Green River samples
318 show the highest UO_2 contents (~700 ppm) and moderate REE. High Th content correlates with
319 high U content. Table 3 summarizes select data for the zircon samples and provides geological
320 and age context, relevant to radiation dosage through time.

321 The average detection limit of the microprobe for UO_2 in zircon is 0.075 wt% UO_2. The
322 Green River sample was the only one that was consistently above detection, while the North
323 Burgess sample had only one analytical point above detection, with the remainder points all
324 below detection but unlikely to be free of uranium. For example, the range of U in Mudtank
325 zircon from the literature is ~5 to 40 ppm (e.g., Currie et al. 1992, Jaeger et al. 2006). The U
326 concentration range of zircon from the St. Peter's Dome area is from 100 to 300 ppm (Smith et
327 al. 1999), however, there is little context for the sample and the geological setting of this region
328 is varied.

329 Zircon formulae were normalized to four anions following Breiter et al. (2006) who
330 studied highly substituted zircon. They noted that this method sometimes resulted in high cation
331 values for the A site, which hosts REE, but that the overpopulation of the A site in their highly
332 substituted samples suggests that some of these cations would be at interstitial sites. The high-
333 REE Mt. Malosa zircon was the only sample of our suite with a high A-site population, but it is
334 in an acceptable range. Kempe et al. (2010) noted that their zircon sample from Mt. Malosa was
335 metamict.

Eudialyte

Content of $(REE+Y)_2O_3$ for the eudialyte samples range from 3.12 to 6.62 wt% and two populations exist based on relative REE content (Appendix C and D). The Kipawa samples show general enrichment of HREE (Tb to Lu, Y) whereas the samples from Mont Saint-Hilaire (MSH) show a dominance of LREE (La to Gd) (Fig. 4). One exception, sample CMNOC478 from MSH, shows an intermediate distribution of REE. Notably, this sample also showed some compositional zoning when using high contrast settings under the SEM, and 15 spots were analyzed on two grains. Three of the analytical points significantly impact the range of standard deviation values, and the points from CMNOC478 show generally elevated REE_2O_3 and MnO with lower CaO and SiO_2. Despite this sample showing some compositional variations, it has been kept within the suite of eudialyte samples primarily because it shows distinct "intermediate" chemistry and higher Nb_2O_5. This distinct character is not related to averaging of compositionally zoned areas.

Total REE content is not appreciably correlated with any other cations, however, relative REE content (LREE/HREE) correlates positively with Mn and negatively with Ca contents. The higher Mn samples also show higher Th and Nb. Thus, the HREE population (Kipawa) shows higher Ca while the LREE population (MSH) shows higher Mn, Th, and Nb. These trends are likely the result of both the compositional environment of formation *and* crystal chemical controls.

Eudialyte formulae were calculated based on the recommendations of Johnsen et al. (2001) of normalizing to 29 cations occupying the M3 and Si(7) sites (Si, Al, Zr, Ti, Nb, Ta) since no structural information is available. This is satisfactory for most of our samples, with REE occupying both Na4 and M1 sites, however, those samples with higher Ca (i.e., from

Kipawa) leave no room in the M1 site for the REE, pushing them all to the Na4 site. Despite this, the high Ca samples of Johnsen and Grice (1999) with accompanying structural data show that Ca and REE both populate the M1 and Na4 sites, and this is likely the case with our high-Ca samples as well.

SPECTRA AND SPECTRAL VARIABILITY

Spectroscopic descriptions of the REE-bearing silicates start with strongly LREE-enriched cerite, followed by mosandrite which is LREE enriched but also hosts HREE. The HREE-rich mineral kainosite is then described, followed by zircon with generally low amounts of U and REE. Finally, a suite of eudialyte samples is presented with examples of both LREE and HREE enrichment.

A brief introduction to the spectroscopic features of each mineral is given, followed by spectra in the VNIR and SWIR ranges (Figs. 5 to 11) and a "Band Index Table" or series of tables (Tables 4 to 10). Regions of spectral features are divided into numbered Clusters, which are outlined and shaded on the index tables. In the case of zircon, the numerous U-related absorptions are divided into Clusters labeled with sequential letters (A, B, C…). Prominent absorption bands are emphasized by shading in the Tables. The Tables also provide an interpretation on the origin of each spectral feature as chosen through comparison with reflectance spectra from unpublished reagent-grade lanthanide oxide spectra, REE-doped calibration standard spectra, and other REE-bearing mineral spectra for which compositional data exists, as well as REE spectroscopy literature. In most cases the confidence in assignments is strong, however, ambiguity is denoted with "?". Some interpretations of absorption bands include multiple causes, typically multiple lanthanides, because of the large number of overlapping multiplets present.

Cerite

Cerite, $Ce_9Fe^{3+}(SiO_4)_6(SiO_3OH)(OH,F)$, is strongly enriched in LREE so its spectral characteristics will be driven mostly by the spectrally active lanthanides Pr^{3+}, Nd^{3+}, and Sm^{3+}. As a silicate with structural OH^- one would also expect vibrational combination and overtone bands. During inspection of the image cube from the cerite hand sample several patches of bastnaesite were identified based on the distinct absorption at 2243 nm, the morphology of the 1080 and 1232 nm Sm^{3+}-related absorptions, and the morphology of the Nd^{3+}-related absorption near 870 nm (as per Turner et al. 2014). The prominent patches were excluded from the VNIR and SWIR pixels used to generate the average spectrum, however, it is likely that some bastnaesite exists with cerite below the spatial resolution of the imaging spectrometers.

The spectrum for cerite in the VNIR range is divided into six clusters (Table 4, Fig. 5). Cluster 1 is an absorption band with its minimum centered at 523 nm. Cluster 2 has one prominent band with its minimum at 583 nm and shoulders near 627, 642, and 661 nm. Cluster 3 is another single band with absorption at 681 nm. Cluster 4 is characterized by a prominent absorption minimum at 746 nm with a weaker absorption at 737 nm and a shoulder at 753 nm. Cluster 5 is similar, showing a prominent absorption minimum at 803 nm with a weaker minimum at 797 nm and shoulders at 811 and 825 nm. Cluster 6 is a prominent doublet with equally strong minima at 864 and 876 nm. A number of weaker absorptions are observed at 888, 898, 945, and 961 nm. All significant features in the VNIR are attributable to Nd^{3+}.

The spectrum for cerite in the SWIR range is divided into five clusters. Cluster 7 shows a shoulder at 1010 nm, followed by a sharp absorption at 1080 nm and accompanying shoulder at 1112 nm. Cluster 8 is another sharp absorption at 1232 nm, followed by a shoulder at 1263. Cluster 9 is a broader collection of absorption features. A narrow absorption is located at 1383

nm, followed by a shoulder at 1408 and a local minimum at 1452 nm. The deepest absorption band occurs at 1540 nm, followed by shoulders at 1578 and 1622 nm. A small but distinct absorption is located at 1710 nm atop a local reflectance high. Cluster 10 is a strong absorption minimum at 1968 nm followed by a shoulder at 2030 nm. Cluster 11 extends from ~2150 out to the end of the spectrometer's range at 2530 nm. The strongest absorptions bands occur at 2193, 2312, and 2424 nm. Shoulders and other weak minima are located at 2243, 2330, 2355, 2380, 2487, and 2518 nm. The weak minimum at 2243 nm is particularly diagnostic of the bastnaesite spectrum, and absorption bands at 2312 and 2330 nm also coincide with bastnaesite. These features are marked on Table 4 and Figure 5 with an asterix and suggest a weak mixed response for the average spectrum from a sub-pixel level.

Mosandrite

Mosandrite, $Ti(□,Ca,Na)_3(Ca,REE)_4(Si_2O_7)_2[H_2O,OH,F]_4*1H_2O$, shows a preference for LREE but also accommodates moderate amounts of HREE and Y. This leads to the spectral signature of mosandrite being dominated by Nd^{3+}, Sm^{3+}, and Pr^{3+} but with influence from Dy^{3+}, Er^{3+}, and Yb^{3+}, its three most abundant HREE. Mosandrite is also host to structural water and hydroxyl according to Bellezza et al. (2009), which results in vibrational absorption bands.

The spectrum for mosandrite in the VNIR range is divided into seven clusters (Table 5, Fig. 6). Cluster 1 is a main absorption at 527 nm with a shoulder near 547 nm. Cluster 2 is a pronounced pair of strong absorption minima centered at 574 and 586 nm, followed by a series of shoulders at 615, 627, and 651 nm. Cluster 3 is a moderate absorption at 681 nm. Cluster 4 contains three strong overlapping absorptions with the strongest minima at 740 nm and flanking absorptions at 736 and 745 nm. Cluster 5 is a strong minimum located at 804 nm with flanking shoulders at 772, 795, and 811 nm. Cluster 6 is an absorption minimum at 874 nm with shoulders

at 864 and 880 nm and two subtle absorptions near 919 and 945 nm. Cluster 7 is a single prominent absorption band at 976 nm.

The spectrum for mosandrite in the SWIR range is divided into five clusters (Table 5, Fig. 6). Cluster 8 is characterized by a strong absorption with a minimum at 1074 nm and a subtle shoulder at 1093 nm. Cluster 9, similarly, has a prominent absorption band at 1257 but a shoulder at the shorter wavelength of 1232 nm. Cluster 10 is a collection of absorptions, starting with shoulders at 1377 and 1440 nm, a strong minimum at 1471 nm, a minimum at 1528 nm, and a shoulder at 1585 nm. Cluster 11 has two shoulders at 1729 and 1817 nm, followed by a strong absorption at 1930 nm. Cluster 12 includes two minima at 2318 and 2462 nm and intermediate shoulders at 2392 and 2418 nm. These absorptions in Cluster 12 are assumed to be combinations and overtones related to bonding amongst H_2O, OH, Ti, and REE.

Kainosite

Kainosite-(Y), $Ca_2Y_2(SiO_3)_4(CO_3)\cdot H_2O$, shows preference for HREE and Y, however, the sample does contain appreciable Nd. Its spectrum is thus driven by absorptions related to Nd^{3+}, Sm^{3+}, Dy^{3+}, and Er^{3+}, with lesser input from other spectrally active lanthanides. Since this mineral contains both water and the CO_3^{2-} radical, absorptions related to vibrational features are also expected.

In the VNIR range, there are six main clusters in the spectrum for kainosite (Table 6, Fig. 7). Cluster 1 occurs near 585 nm and comprises three weak absorptions, however, there is considerable noise in this region given the relatively smaller number of pixels in the ROI. Cluster 2 is a single and relatively broad absorption at 651 nm. Cluster 3 is a main absorption at 750 nm flanked by absorption minima at 737 and 754 nm along with several shoulders. Cluster 4 is a

strong absorption located at 805 nm with notable flanking local minima. Cluster 5 contains two main absorptions located at 865 and 876 nm, followed by two other weaker and noisy absorptions at 887 and 896 nm. Cluster 6 has a single absorption at 978 nm.

In the SWIR range, there are seven main clusters in the spectrum for kainosite (Table 6, Fig. 7). Cluster 7 is a prominent absorption minimum at 1080 nm followed by two shoulders at 1105 and 1156 nm. Cluster 8 is two sharp absorptions with minima at 1232 and 1263 nm followed by a weaker shoulder at 1288 nm. Cluster 9 contains a single band at 1377 nm. Cluster 10 is one main absorption at 1484 nm with flanking absorptions at 1415 and 1528 nm. Cluster 11 has a series of weak minima and shoulders stretching from ~1560 to ~1865 nm, with the most prominent at 1653 and 1723 nm. The absorptions are nearing the level of noise present in the spectrum (22 pixels were averaged), but they are reported as candidate bands since lanthanides are responsible for numerous fine bands in this wavelength region. Cluster 12 comprises two strong overlapping absorptions centered at 1961 and 2055 nm with a shoulder at 2105 nm. Cluster 13 consists of a series of absorption minima and shoulders out to 2530 nm, with the strongest at 2387 and 2474 nm. These absorptions are assumed to be combinations and overtones related to bonding amongst CO_3, OH, and REE.

Zircon

The main variables driving the spectrum of zircon ($ZrSiO_4$) are U^{4+}, U^{5+}, a crystalline versus amorphous matrix, REE^{3+} content, and OH/H_2O bands. From this perspective, three spectral classes of zircon are evident that correlate with their chemistry: U-bearing (North Burgess, Green River, Mudtank), high REE with U (Mt. Malosa), and metamict (St. Peters Dome). Band index Tables have been split into the VNIR and SWIR to accommodate the multiple samples and the inclusion of uranium-related spectral features.

Absorption spectra for zircon are primarily described using the Green River sample for high U and the Mt. Malosa sample for high REE as they both display prominent features (Table 7, Figs. 8 and 9). The remaining samples (North Burgess, Mudtank, and St. Peters Dome) show subdued absorptions in the same regions for U, and only slight absorptions for REE. Note that weak REE features are still present in the Green River samples and conversely, weak U features are still present in the Mt. Malosa sample.

In the VNIR range there are five main absorptions in the Green River spectra that are related to uranium and labeled A through E (Figs. 8 and 9). The strongest of these are at 654 (A) and 916 (D) nm, while weaker bands occur at 690 (B), 849 (C), and 961 (E) nm. The absorption near 654 nm also overlaps with a band ascribed to Er^{3+}. The Mt. Malosa sample has six main REE-related absorption clusters (Figs. 8 and 9). Cluster 1 shows moderate absorption bands at 576 and 582 nm. Cluster 2 is a series of three weak bands at 651, 660, and 681 nm. Cluster 3, the first of three prominent absorption clusters, has strongest band minima at 739 and 750 nm with a weak minimum at 757 nm and two shoulders. Cluster 4 has a prominent band at 808 nm, exhibits shoulders at shorter and longer wavelengths, and also shows two weak and noisy absorptions at 835 and 844 nm. Cluster 5 is characterized by three absorption bands with minima at 870, 880, and 893 nm. Cluster 6 contains a single band located at 978 nm.

Three spectral classes of zircon are evident in the SWIR: U-bearing (North Burgess, Green River, Mudtank), high REE with U (Mt. Malosa), and metamict (St. Peters Dome). All absorption features in the Mudtank and North Burgess spectra can be related to U^{4+}, U^{5+}, and OH/H_2O (Table 8, Figs. 8 and 9). The Green River sample has a nearly identical set of absorptions related to U^{4+} and U^{5+}, but also a few subtle REE^{3+}-related absorptions. The Mt. Malosa sample shows a collection of REE-related bands but also shows strong influence from

the strongest U-related absorption clusters, G and I. The St. Peter's Dome zircon is the most featureless, however, weak absorption bands occur at all the appropriate wavelengths for U and sometimes REE, suggesting low concentrations of REE, U^{4+}, and U^{5+} in a host matrix that is poorly crystalline. Its strongest bands occur at 1415, 1924, and 2206 nm, all related to H_2O/OH.

There are eight clusters in the Green River, Mudtank, and North Burgess samples that are associated with uranium (labeled F through M). Cluster F is a band at 1061 nm with a shoulder at 1010 nm. Cluster G shows an absorption minimum at ~1118 nm related to U^{5+} and another band near 1143 nm related to U^{4+} that is expressed as a shoulder. Cluster H shows two distinct and overlapping bands at 1326 and 1345 nm. Cluster I is similar and shows a strong U^{5+}-related absorption minimum at 1503 nm with adjacent weaker U^{4+}-related bands at 1478 and 1534 nm that are influenced by Er^{3+} and Sm^{3+} absorptions. Cluster J contains a distinct minimum at 1660 nm and a second at 1704 nm. Cluster K has a weak shoulder near 1792 nm and Cluster L is a prominent single band located near 2074 nm. Cluster M is a weak shoulder at 2187 nm, however, it is not apparent in the Green River spectrum.

Using the Mt. Malosa sample as a reference, another seven clusters are distinguished for zircon in the SWIR range. Cluster 7 is a pair of absorption minima at 1086 and 1105 nm. Cluster 8 is a strong absorption feature with two minima at 1244 and 1263 nm flanked by shoulders at 1200 and 1288 nm. Cluster 9 includes two absorption minima located at 1389 nm and 1415 nm. Cluster 10 overlaps with the uranium-related "Cluster I" and includes shoulders at 1427 and 1528 nm, plus additional absorption minima at 1560 and 1616 nm. Cluster 11 shows a weak minimum at 1691 nm and a more moderate minimum located at 1729 nm. Cluster 12 comprises two overlapping bands: low-REE samples have minima near 1924 nm while the high-REE sample (Mt. Malosa) has a shoulder at 1917 nm and a minimum pushed out to 1943 nm.

519 Absorption features related to H_2O/OH are best exhibited by the St. Peters Dome sample.
520 Strong bands are located at 1415, 1924, and 2206 nm. Finally, for Cluster 13 a number of
521 absorption minima and shoulders are recorded from ~2205 nm out to 2530 nm, however, at this
522 point they are tentatively ascribed to combinations and overtones related to H_2O, OH, and the
523 variably metamict host lattice (i.e., Zr, Si, U, REE).

524 **Eudialyte**

525 Eudialyte, $Na_{15}Ca_6(Fe^{2+},Mn^{2+})_3Zr_3Si[Si_{25}O_{73}](O,OH,H_2O)_3(OH,Cl)_2$, has a flexible and
526 complicated crystal structure and can show varied chemistry. The samples studied here from
527 Kipawa and Mont Saint-Hilaire (MSH) can be split into two groups based on their ratio of LREE
528 to HREE ("L/H") but generally share most spectral features. The Kipawa samples show
529 enrichment of HREE (Tb to Lu, Y) whereas the eudialyte samples from MSH show a greater
530 occupation by LREE (La to Gd). One exception, sample CMNOC478 from MSH, shows an
531 intermediate distribution of REE. Consequently, the high-LREE samples will be dominated by
532 spectral features from Nd^{3+}, Pr^{3+}, and Sm^{3+}, while the high-HREE samples will be dominated by
533 spectral features from Dy^{3+}, Er^{3+}, and Yb^{3+} but influenced by Nd^{3+}. In the LREE-enriched group
534 sample CMN88-79 (Pinch) shows the highest concentration of LREE and in the HREE group
535 sample Kipawa-Mariano shows the greatest concentration of HREE (and smallest LREE/HREE
536 value). Notable, however, is that sample CMNOC37104 shows the largest LREE/HREE value
537 but only contains 4.07 wt% REE_2O_3. The high-HREE samples are also bright red to pink in color
538 indicating a strong presence of $^{IV}Fe^{2+}$, however, all samples have approximately the same
539 amount of iron with the exception of CMNOC2045 (6.55 wt% FeO). $^{IV}Fe^{2+}$ produces absorptions
540 near 530 and 1365 nm while $^{V}Fe^{2+}$ will generate absorptions near 917 and 2500 nm. The LREE

541 samples also show higher Mn contents, however, the associated electronic transitions will only
542 affect the region from ~345 to 535 nm.

543 Band index Tables for eudialyte in the VNIR and SWIR ranges have been split into the
544 two groupings as defined by the LREE/HREE ratio. The "LREE group" comprises samples
545 CMNOC2045, CMNOC476, CMN88-79 (Pinch), CMN72-24, and CMNOC37104, while the
546 "HREE group" comprises all three Kipawa samples (Mariano, UofA, and F92-23) as well as
547 CMNOC478 because of its moderate Dy content, despite having LREE/HREE>1. The maximum
548 "peak" reflectance in the region between 1050 and 1400 nm is also given and described in the
549 text.

550 Spectra for eudialyte in the VNIR range (Tables 9 and 10, and Figs. 10 and 11) are
551 divided into six clusters for all samples, however, not all samples display all spectral features.
552 Cluster 1 comprises two absorptions near 576 and 584 nm in a region that is typically steeply
553 sloped with minor noise. It is only observed in samples with higher LREE content. Cluster 2,
554 prominent in the HREE group, is also located in a region that is typically steeply sloped and
555 consists of a main absorption band at 651 nm with a weak minimum at 661 and shoulder at 680
556 nm. Cluster 3 in the HREE group comprises a central absorption minimum near 745 nm with
557 flanking local minima near 735 and 752 nm. In the LREE group this cluster is a doublet
558 characterized by a moderate minimum near 739 nm followed by another minimum near 751 nm.
559 Cluster 4 in the HREE group is a strong absorption minimum at 800 nm followed by a weaker
560 minimum near 808 nm. In the LREE group this cluster is expressed as another doublet with a
561 typically weaker band near 798 nm and a stronger band near 807 nm. Cluster 5 is most
562 prominent in the HREE group and consists of a principal absorption minimum near 873 nm and a
563 broad absorption at 910 nm with several other weak intermediate shoulders. In the LREE group

it is characterized by two minima near 866 and 880. Cluster 6 is only observed in the HREE group and it consists of a single strong absorption at 974 nm. In addition to the six clusters, the approximate band center is given for samples that show evidence of $^{V}Fe^{2+}$ in the form of a very broad absorption centered near 915 nm.

Spectra for eudialyte in the SWIR range are divided into four clusters (Tables 9 and 10, and Figs. 10 and 11). Cluster 7 includes a weak absorption near 1061 nm typically expressed as a shoulder, followed by a weaker shoulder near 1099 nm. Cluster 8 is the most prominent absorption with the most complexity and stretches from ~1115 to 1615 nm. The deepest absorption for all samples occurs near 1433 nm. The LREE group samples are then characterized by a series of shoulders at both shorter and longer wavelengths. Notably, CMNOC2045, CMNOC476, and CMN88-79 (Pinch) each exhibit an absorption at 1408 nm expressed as a shoulder, while CMNOC37104 and CMN72-24 do not show this absorption band at all. In the HREE group additional distinct absorption minima occur at 1276, 1408, and 1534 nm, as well as more subtle shoulders across the whole cluster. This region is also the general location of a documented $^{IV}Fe^{2+}$-related band centered near 1366 nm (Polshin et al. 1991), however, this is hard to objectively observe in our spectra. Cluster 9 is a sharp absorption band at 1930 nm along with several shoulders. Cluster 10 ranges from 2150 nm out to the full range of the spectrometer (2530 nm). In the LREE group the strongest absorptions occur near 2437 and 2480 nm while the HREE group has its strongest band near 2437 nm with a consistent shoulder at 2493 nm. Within the LREE group, samples CMN72-24 and CMNOC37104 also have an additional distinct absorption at 2249 nm. In addition to the five clusters in the SWIR, each eudialyte sample also shows a maximum reflectance between 1050 and 1400 nm.

DISCUSSION

Compilation of REE-bearing silicate mineral spectra

The REE-bearing silicate minerals studied here show a large diversity of overall crystal structures, chemical compositions, and host sites for Ln^{3+}. The mineral suite included samples that are LREE-dominant (e.g., cerite), HREE-dominant (e.g., kainosite), and less selective but still with high REE content (e.g., mosandrite). REE are incorporated as trace elements (e.g., zircon), major substitutions (e.g., eudialyte), and structural components (e.g., kainosite). The mineral suite also included samples with structural H_2O, structural OH, structural CO_3, unusually coordinated Fe, and probable extensive radiation damage. Figure 12 compiles representative reflectance spectra and displays the wide range of expected spectral variability.

The reflectance spectrum for cerite is dominated by spectrally active LREE. The reflectance spectrum for mosandrite is dominated by spectrally active LREE with influence from Er^{3+} and Yb^{3+}. The reflectance spectrum for kainosite is dominated by spectrally active HREE, however, the 2055 nm absorption is unusually strong. This band is aligned for potential input from Pr^{3+}, Eu^{3+}, Tb^{3+}, and Ho^{3+} electronic transitions but none of these elements are present in any great amount. Another possibility is U^{4+} despite EMPA results below the detection limit of 0.075 wt% UO_2, however, the zircon samples with U below detection still show strong U absorptions. Finally, the formula for kainosite includes structural water, SiO_4 tetrahedra, and carbonate radicals which could provide the appropriate vibrational combinations or overtones in this region.

Zircon reflectance spectra exhibit strong absorption bands for U^{4+} and U^{5+} despite generally low concentrations (<750 ppm). The high-REE and low-U sample from Mt. Malosa

608 and the low-REE and high-U sample from Green River provide excellent complementary
609 baseline spectra for zircon.

610 The eudialyte sample suite shows a range of compositions and comprised nine samples
611 from two localities. Reflectance spectroscopy in the VNIR-SWIR range was able to distinguish
612 LREE-enriched from HREE-enriched samples despite overlapping VNIR absorption clusters
613 related to Nd^{3+} (LREE group) and Dy^{3+} (HREE group). Variability was observed in absorption
614 minima wavelength positions, which is possibly tied to the complex structure of this diverse
615 mineral group. Evidence of $^{IV}Fe^{2+}$ and $^{V}Fe^{2+}$ was observed in the VNIR and SWIR ranges, and in
616 concert with Dy^{3+}-related absorptions in the SWIR has a large influence on the location of
617 maximum reflectance between ~1050 and 1400 nm. A larger and more diverse sample set would
618 provide greater confidence for implementing this metric.

619 Preference of a mineral for LREE or HREE and the resulting distribution in a given
620 sample will define which spectrally active lanthanides are present, and therefore what the overall
621 4*f*-4*f* transition-related spectral pattern will be. Of the REE silicates, cerite is a good
622 representative of LREE-enrichment, kainosite represents HREE-enrichment, and mosandrite and
623 eudialyte display good compositional ranges. The two zircon samples shown in Figure 12
624 represent high U and high REE examples and display sharp and diagnostic spectral features.

625 **Spectral patterns of eudialyte**

626 The eudialyte samples roughly form two groups based on the LREE/HREE value.
627 Sample CMNOC478 is LREE-enriched but also shows the most Dy content of that group. The
628 larger number of samples for this mineral allows for greater intramineral comparisons, however,
629 its flexible and complex crystal structure also allows for significant variations in reflectance

spectroscopy. The following comparisons are made mostly based on the two LREE/HREE groups (Figs. 10 and 11).

Morphology of the absorption clusters near 745 and 800 nm allow LREE (Nd)-rich samples to be distinguished from HREE (Dy, Er, Ho)-rich samples. The Nd^{3+} signal in eudialyte is expressed as two 'doublets'. Near 745 nm, the shorter of the two wavelength absorptions (741 and 752 nm) is usually stronger, and near 800 nm the longer of the two wavelength absorption (800 and 810 nm) is usually stronger. For HREE-enriched samples, Dy^{3+}, Er^{3+}, and Ho^{3+} absorptions combine so that near 745 nm there is a central absorption *at* or close to 745 nm flanked by two absorption minima. At 800 nm an asymmetrical cluster is present with a central strong absorption band followed by several weaker absorptions at longer wavelengths that are typically expressed as shoulders or local minima out to ~825 nm. The HREE group also show a Dy^{3+}-related absorption at 910 nm and an Er^{3+}-Yb^{3+}-related absorption near 974 nm.

Two spectra emphasize the impact that coordination state of iron has on reflectance spectra of eudialyte. Sample CMNOC2045 shows the least resolved LREE features in the VNIR, however, this is not due to lower Nd but rather its high proportion of $^{V}Fe^{2+}$ (6.55 wt%) that causes a very strong absorption band centered near 920 nm and which stretches from ~700 nm out past 1000 nm (see Fig. 10, unstacked reflectance). This sample also shows lower reflectance in the SWIR, particularly at longer wavelengths. The lowest Nd-bearing sample in the LREE group is CMNOC476, which actually shows well-resolved Nd^{3+}-related features owing to iron predominantly in square-planar coordination ($^{IV}Fe^{2+}$) and therefore less absorption (greater reflectance) from ~700 to 1000 nm, allowing for more contrast where Nd^{3+} shows absorption bands. Unsurprisingly, this sample shows red coloration due to its high $^{IV}Fe^{2+}$.

All eudialyte samples have a reflectance maximum in the SWIR somewhere between 1050 and 1400 nm (Fig. 11). Qualitatively, this is related to the influence of Dy^{3+} (and to a lesser degree Sm^{3+}) which has its strongest absorption near 1290 nm and a series of absorptions at shorter wavelengths back out to ~1085 nm. It is also due to the influence of square planar $^{IV}Fe^{2+}$, which has a prominent broad absorption centered at 1366 nm (Polshin et al. 1991). In our sample suite it conveniently divides the high HREE and high $^{IV}Fe^{2+}$ samples from the high LREE and high $^{V}Fe^{2+}$ samples based on the location of the reflectance maximum – the samples from Kipawa (HREE, $^{IV}Fe^{2+}$) show maxima below 1200 nm while the MSH (LREE, $^{V}Fe^{2+}$) samples show maxima beyond 1200 nm and typically beyond 1300 nm.

The absorption at ~1433 nm (6978 cm^{-1}) within Cluster 8 is attributed to H_2O and/or OH in the crystal structure as it is present across all samples in a similar manner as the ~1930 nm absorption. The absorption at 1408 nm (7102 cm^{-1}) is present as a local minimum in the samples from Kipawa, a shoulder in samples CMN88-79, CMNOC476, and CMNOC 2045, and is absent in the CMN72-24, CMNOC37104, and CMONC478 spectra. In this region there is the possibility of a narrow Sm^{3+}-related absorption, however, the Kipawa samples have lower Sm than the MSH samples, which do not display this resolved absorption band. The absorption at 1408 nm suggests that (1) an additional and distinct H_2O- or OH-related absorption is present in the high HREE Kipawa samples, (2) an H_2O or OH-related absorption near 1408 nm in the MSH samples is broadened to the point that it cannot be resolved, or (3) that the H_2O- or OH-related absorption near 1408 nm is shifted in the MSH samples to a longer wavelength that overlaps with the 1433 nm absorption. This pattern also parallels the shift in reflectance maximum (Fig. 11). Additional infrared spectroscopy and crystal structure studies would be needed to satisfactorily resolve this question.

675 A notable variation within these groups is a subclass of high Mn/low Fe samples
676 (CMN72-24 and CMNOC37104) within the LREE-enriched samples. Samples 37104 and
677 CMN72-24 have district variations to their spectra. They do not show strong absorptions related
678 to $^{IV}Fe^{2+}$ or $^{V}Fe^{2+}$, which is consistent with their low Fe contents. They also show the highest
679 LREE/HREE values, highest Mn, and highest U. In the SWIR range, the absorption band at 1408
680 nm is missing, and they possess strong bands at 2249 nm that are unlike any other samples.

681 Applying the results of this study to five eudialyte spectra from the Red Wine Complex
682 in Kerr et al. (2011), suggests their samples would likely be LREE-enriched and $^{IV}Fe^{2+}$-
683 dominant. In a separate report, Kerr (2011) reviewed the mineralization at the Red Wine
684 Complex and provided a chondrite-normalized plot of eudialyte ore that supports this
685 interpretation, as well as photographs of pink eudialyte.

686 **The Er-Yb related absorption near 978 nm**

687 The ~978 nm absorption due to Er^{3+} and Yb^{3+} is an important factor for mineral
688 identification of HREE-bearing samples because of its sensitivity to the mineral host. High Er
689 and Yb alone will not drive the absorption near 978 nm – the "fit" of Er^{3+} and Yb^{3+} at the
690 substitutional site appears to play a strong role, and asymmetry and ligand identity are likely
691 factors as well. Eudialyte and mosandrite spectra show comparable absorption strengths and
692 Er+Yb concentrations (Figure 13). Zircon samples for the displayed spectra host considerably
693 lower Er and Yb contents yet still provide discernable absorptions. Kainosite, however, contains
694 a much greater amount of Er and Yb, but shows only a poorly resolved and weak absorption
695 band.

Table 11 tabulates key cation site parameters to assess how well Yb^{3+} and Er^{3+} cations fit at sites of the various minerals. In kainosite REE^{3+} are hosted at a designated REE site in eight-fold coordination with oxygen. In zircon REE^{3+} are hosted in the ZrO_8 dodecahedron. For mosandrite, REE^{3+} are hosted at three sites with mixed cation populations. The M4 and M5 sites are in seven-fold coordination with six oxygen atoms and one OH^- molecule and can be thought of as being dominated by Ce^{3+} and Ca^{2+}, while the third site, M3, is in six-fold coordination with two oxygen and four mixed anion sites and in our sample is dominated by Na^+. In eudialyte REE^{3+} are hosted at two sites with mixed cation populations, M1 and Na4. The M1 site is in six-fold coordination with oxygen and is dominated by Ca^{2+}, while the second cavity-like site (Na4) is generally in nine-fold coordination with mixed anions and is occupied by Na^+. Comparing the valence charge and ionic radius of the "normal" cation site occupants against the character of Yb^{3+} in that same site gives a first approximation of "fit". Yb^{3+} is a particularly poor fit for the Zr site in zircon, the M3 site in mosandrite and the Na4 site in eudialyte, whereas the kainosite structure shows a very good fit for Yb^{3+} at the Y^{3+} site. Descriptively for zircon, $^{VIII}Yb^{3+}$ is forced into a polyhedron where it has a larger ionic radius than the "displaced" and more strongly charged $^{VIII}Zr^{4+}$. The resulting absorption strength relative to Er+Yb concentration (i.e., the absorption coefficient) is thus relatively high because of the "misfit".

For minerals that can be either LREE- or HREE-enriched, this Er^{3+}-Yb^{3+} related absorption can be quite useful. In eudialyte it can be used to discriminate high-LREE versus high-HREE samples, and the absorption also exhibits wavelength shifts that can be exploitable for mineral identification (974 nm in eudialyte, 976 nm in mosandrite, ~978 nm in kainosite, and 978/979 nm in zircon) (Figure 13). Similar patterns are evident in the reflectance spectra of the REE-phosphate minerals monazite, xenotime, and britholite.

719 **Absorption band variations amongst REE-bearing silicate minerals**

720 Variations are observed for several of the REE^{3+}-related absorption bands amongst the
721 various minerals. Some of these variations are nearing the spectral resolution of the
722 spectrometer, making them hard to distinguish from noise, and others are located on the flanks of
723 steeper slopes of the spectra, making their 'shift' perhaps just an artifact of the overall
724 continuum. Nevertheless, some clusters of absorptions show strong changes in both relative
725 strengths between related absorptions and band center positions. Figure 14 shows an example of
726 this in the VNIR, but greater investigations are warranted with an expanded set of REE-bearing
727 minerals.

728 **IMPLICATIONS**

729 We report the first reflectance spectra for cerite, mosandrite, and kainosite and are
730 accompanied by microanalytical characterization. We also report the first set of reflectance
731 spectra for eudialyte with supporting microanalytical characterization. Although reflectance
732 spectra of zircon are available in the literature, we report the first systematic investigation of U-
733 enriched and REE-enriched samples with accompanying microanalytical characterization.
734 Importantly, the REE-bearing silicate minerals of this study display spectral characteristics in the
735 VNIR-SWIR range that enable their discrimination and would thus allow for their automated
736 detection and recognition. This includes the notable observation that some specific REE^{3+}-related
737 absorption bands can undergo wavelength shifts and changes in relative intensities between
738 different minerals, and that these changes are not solely related to varying contents of specific
739 lanthanides.

ACKNOWLEDGEMENTS

Tony Mariano and Michel Picard (Canadian Museum of Nature) are thanked for their help with acquiring samples, and Jilu Feng and Steve Creighton for their help with data collection. Financial support is acknowledged from the Natural Sciences and Engineering Research Council of Canada.

REFERENCES

Badenes, J. A., Vicent, J. B., Llusar, M., Tena, M. A., and Monr, G. (2002) The nature of Pr-$ZrSiO_4$ yellow ceramic pigment. Journal of Materials Science, 37, 1413-1420.

Baldridge, A. M., Hook, S. J., Grove, C. I., and Rivera, G. (2009) The ASTER spectral library version 2.0. Remote Sensing of Environment, 113, 711-715.

Baur, W. H. (1974) The geometry of polyhedral distortions. Predictive relationships for the phosphate group. Acta Crystallographica Section B: Structural Crystallography and Crystal Chemistry, 30, 1195-1215.

Bellezza, M., Merlino, S., and Perchiazzi, N. (2009) Mosandrite: Structural and crystal-chemical relationships with rinkite, The Canadian Mineralogist, 47, 897-908.

Braun, S. A., Bream, B. R., and Gualda, G. A. (2009) Age and chemistry of megacrystic zircons from Zirconia, North Carolina. In: 2009 Portland GSA Annual Meeting Conference Proceedings.

Breiter, K., Förster, H. J., and Škoda, R. (2006) Extreme P-, Bi-, Nb-, Sc-, U-and F-rich zircon from fractionated perphosphorous granites: The peraluminous Podlesí granite system, Czech Republic. Lithos, 88, 15-34.

761 Burns, R. (1996) Mineralogical Applications of Crystal Field Theory, Second Edition,
762 Cambridge University Press, Cambridge, 551 p.

763 Clark, R. N., Swayze, G. A., Wise, R. A., Livo, K. E., Hoefen, T. M., Kokaly, R. F., and Sutley,
764 S. J. (2007) USGS digital spectral library splib06a, U.S. Geol. Surv. Digital Data Ser.
765 231p.

766 Currie, J. (1951) The occurrence and relationships of some mica and apatite deposits in
767 southeastern Ontario. Economic Geology, 46, 765-778

768 Currie, K. L., Knutson, J., and Temby, P. A. (1992) The Mud Tank carbonatite complex, central
769 Australia—an example of metasomatism at mid-crustal levels. Contributions to
770 Mineralogy and Petrology, 109, 326-339.

771 Eby, G.N., Roden-Tice, M., Krueger, H.L., Ewing, W., Faxon, E.H. and Woollley, A.R. (1995)
772 Geochronology and cooling history of the northern part of the Chilwa Alkaline Province,
773 Malawi. Journal of African Earth Sciences, 20, 275-288.

774 Fielding, P.E. (1970) The distribution of uranium, rare earths, and color centers in a crystal of
775 natural zircon. American Mineralogist, 55, 428-440.

776 Finch, R. J., and Hanchar, J. M. (2003) Structure and chemistry of zircon and zircon-group
777 minerals. Reviews in Mineralogy and Geochemistry, 53, 1-25.

778 Finch, R. J., Hanchar, J. M., Hoskin, P. W. O., and Burns, P. C. (2001) Rare-earth elements in
779 synthetic zircon: Part 2. A single-crystal X-ray study of xenotime substitution, American
780 Mineralogist, 86, 681-689.

781 Friis, H., Finch, A. A., Williams, C. T., and Hanchar, J. M. (2010) Photoluminescence of zircon
782 ($ZrSiO_4$) doped with REE^{3+} (REE= Pr, Sm, Eu, Gd, Dy, Ho, Er) Physics and Chemistry of
783 Minerals, 37, 333-342.

784 Guastoni, A., Nestola, F., and Giaretta, A. (2009) Mineral chemistry and alteration of rare earth
785 element (REE) carbonates from alkaline pegmatites of Mount Malosa, Malawi. American
786 Mineralogist, 94, 1216-1222.

787 Hanchar, J. M., Finch, R. J., Hoskin, P. W., Watson, E. B., Cherniak, D. J., and Mariano, A. N.
788 (2001) Rare earth elements in synthetic zircon: Part 1. Synthesis, and rare earth element
789 and phosphorus doping. American Mineralogist, 86, 667-680.

790 Hancock, L., Kirkland, C.L., and Huntington, J. (2012) Hyperspectral data – a tool for
791 identification of geological chronometers. In 34th International Geological Conference
792 (IGC) Australian Geosciences Council.

793 Hansen, S., Mosel, B. D., Müller-Warmuth, W., and Fielding, P. E. (1996) EPR studies of Tb^{4+}
794 in single crystals of zircon and scheelite structure silicates and germanates. Zeitschrift fur
795 Naturforschung A-Journal of Physical Sciences, 51, 885-894.

796 Hoefen, T. M., Swayze, G., Giles, S.A., Van Gosen, B.S., Emsbo, P., and Karst, A. (2013)
797 Spectroscopic Investigations of REE hosted heavy mineral sands and phosphates.
798 In Geological Society of America Abstracts with Programs, 45, 278.

799 Jaeger, H., Pletzke, K. and Hanchar, J. M. (2006) Hyperfine Interaction Study of Short Range
800 Order in Zircon. Environmental Issues and Waste Management Technologies in the
801 Ceramic and Nuclear Industries IX, 155, 31 – 40.

802 Johnsen, O., and Grice, J. D. (1999) The crystal chemistry of the eudialyte group, The Canadian
803 Mineralogist, 37, 865-891.

804 Johnsen, O., Ferraris, G., Gault, R. A., Grice, J. D., Kampf, A. R., and Pekov, I. V. (2003) The
805 nomenclature of eudialyte-group minerals, The Canadian Mineralogist, 41, 785-794.

806 Kempe, U., Thomas, S. M., Geipel, G., Thomas, R., Plötze, M., Böttcher, R., and Trinkler, M.
807 (2010) Optical absorption, luminescence, and electron paramagnetic resonance (EPR)
808 spectroscopy of crystalline to metamict zircon: Evidence for formation of uranyl,
809 manganese, and other optically active centers. American Mineralogist, 95, 335-347.

810 Kerr, A. (2011) Rare-earth element (REE) mineralization in Labrador: A review of known
811 environments and the geological context of current exploration activity. In: Current
812 Research Newfoundland and Labrador Department of Natural Resources, Geological
813 Survey Report 11-1, 109-143.

814 Kerr, A., Rafuse, H., Sparkes, G., Hinchey, J., and Sandeman, H. (2011) Visible/Infrared
815 spectroscopy (VIRS) as a research tool in economic geology: background and pilot studies
816 from Newfoundland and Labrador. In: Current Research, Newfoundland and Labrador
817 Department of Natural Resources Geological Survey Report 11-1, 145-166.

818 Klinger, M., Kempe, U., Pöppl, A., Böttcher, R., and Trinkler, M. (2012) Paramagnetic hole
819 centres in natural zircon and zircon colouration. European Journal of Mineralogy, 24,
820 1005-1016.

821 Krupa, J. C., and Carnall, W. T. (1993) Electronic structure of U^{4+}, Np^{4+}, and Pu^{4+} doped into
822 $ThSiO_4$ single crystal. The Journal of Chemical Physics, 99, 8577-8584.

Kruse, F. A., Lefkoff, A. B., Boardman, J. W., Heidebrecht, K. B., Shapiro, A. T., Barloon, P. J., and Goetz, A. F. H. (1993) The spectral image processing system (SIPS)—interactive visualization and analysis of imaging spectrometer data. Remote Sensing of Environment, 44, 145-163.

Laruhin, M. A., Van Es, H. J., Bulka, G. R., Turkin, A. A., Vainshtein, D. I., and Den Hartog, H. W. (2002) EPR study of radiation-induced defects in the thermoluminescence dating medium zircon ($ZrSiO_4$). Journal of Physics: Condensed Matter, 14, 3813.

Mariano, A.N., and Mariano, A. (2012) Rare earth mining and exploration in North America. Elements, 8, 369-376.

McDonough, W. F., and Sun, S. (1995) The composition of the Earth. Chemical Geology, 120, 223-254.

Moore, P. B., and Shen, J. (1983) Cerite, $RE_9(Fe^{3+},Mg)(SiO_4)_6(SiO_3OH)(OH)_3$: its crystal structure and relation to whitlockite. American Mineralogist, 68, 996-1003.

Momma, K., and Izumi, F. (2011) VESTA 3 for three-dimensional visualization of crystal, volumetric and morphology data. Journal of Applied Crystallography, 44, 1272-1276.

Nasdala, L., Zhang, M., Kempe, U., Panczer, G., Gaft, M., Andrut, M., and Plötze, M. (2003) Spectroscopic methods applied to zircon. Reviews in Mineralogy and Geochemistry, 53, 427-467.

Neave, D. A., Black, M., Riley, T. R., Gibson, S. A., Ferrier, G., Wall, F., and Broom-Fendley, S. (2016) On the feasibility of imaging carbonatite-hosted rare earth element deposits using remote sensing. Economic Geology, 111, 641-665.

Pakhomovsky Y A, Men'shikov Y P, Yakovenchuk V N, Ivanyuk G Y, Krivovichev S V, Burns P C (2002) Cerite-(La), $(La,Ce,Ca)_9(Fe,Ca,Mg)(SiO_4)_3[SiO_3(OH)]_4(OH)_3$, a new mineral species from the Khibina alkaline massif: Occurrence and crystal structure. The Canadian Mineralogist, 40, 1177-1184.

Polshin, E. V., Platonov, A. N., Borutzky, B. E., Taran, M. N., and Rastsvetaeva, R. K. (1991) Optical and Mössbauer study of minerals of the eudialyte group. Physics and Chemistry of Minerals, 18, 117-125.

Richman, I., Kisliuk, P., and Wong, E. Y. (1967) Absorption Spectrum of U^{4+} in Zircon ($ZrSiO_4$). Physical Review, 155, 262-263.

Rossman, G. R., and Taran, M. N. (2001) Spectroscopic standards for four-and fivefold-coordinated Fe^{2+} in oxygen-based minerals. American Mineralogist, 86, 896-903.

Rumanova I M, Volodina G F Belov N V (1967) The crystal structure of the rare earth ring silicate kainosite $Ca_2(Y,Tr)_2[Si_4O_{12}]\ CO_3 \cdot H_2O$. Soviet Physics – Crystallography, 11, 485-491

Shannon, R.D. (1976) Revised effective ionic radii and systematic studies of interatomic distances in halides and chalcogenides. Acta Crystallographica, A32, 751–767.

Sheard, E. R., Williams-Jones, A. E., Heiligmann, M., Pederson, C., and Trueman, D. L. (2012) Controls on the concentration of zirconium, niobium, and the rare earth elements in the Thor Lake rare metal deposit, Northwest Territories, Canada. Economic Geology, 107, 81-104.

Smith, D. R., Noblett, J., Wobus, R. A., Unruh, D., Douglass, J., Beane, R., Davis, C., Goldman, S., Kay, G., Gustavson, B., Saltoun, B., and Stewart, J., (1999) Petrology and geochemistry of late-stage intrusions of the A-type, Mid-Proterozoic Pikes Peak batholith (central Colorado, USA): implications for petrogenetic models. Precambrian Research 98, 271-305

Sokolova, E., and Cámara, F. (2008) From structure topology to chemical composition. VIII. Titanium silicates: the crystal chemistry of mosandrite from type locality of Låven (Skådön), Langesundsfjorden, Larvik, Vestfold, Norway. Mineralogical Magazine, 72, 887-897.

Swayze, G.A., Pearson, N., Wilson, S., Benzel, W.M., Clark, R., Hoefen, T.M., Van Gosen, B., Adams, M., and Reitman, J. (2013) Spectrally distinguishing between REE-bearing minerals based on differences in their crystal field *f-f* transition absorptions. In Geological Society of America Abstracts with Programs, 45, 278.

Turner, D. J., Rivard, B., and Groat, L. A. (2014) Visible and short-wave infrared reflectance spectroscopy of REE fluorocarbonates. American Mineralogist, 99, 1335-1346.

Turner, D. J., Rivard, B., and Groat, L. A. (2016) Visible and short-wave infrared reflectance spectroscopy of REE phosphate minerals. American Mineralogist, 101, 2264-2278.

Vance, E. R., and Mackey, D. J. (1978) Optical spectra of U^{4+} and U^{5+} in zircon, hafnon, and thorite. Physical Review B, 18, 185.

Zhang, M., Salje, E. K., and Ewing, R. C. (2002) Infrared spectra of Si-O overtones, hydrous species, and U ions in metamict zircon: radiation damage and recrystallization. Journal of Physics: Condensed Matter, 14, 3333.

885 Zhang, M., Salje, E. K., and Ewing, R. C. (2003) Oxidation state of uranium in metamict and
886 annealed zircon: near-infrared spectroscopic quantitative analysis. Journal of Physics:
887 Condensed Matter, 15, 3445.

888

889 **FIGURE CAPTIONS**

890 Figure 1. Coordination polyhedra for Ln^{3+} in various REE-bearing silicates. Top row includes
891 polyhedra for zircon (Zr site, coordinated by eight oxygen atoms), kainosite (REE site,
892 coordinated by eight oxygen atoms), and cerite (three distinct but similar sites coordinated by
893 eight oxygen atoms and one OH^- molecule). The middle row includes the two sites in eudialyte,
894 M1 (left, coordinated by six oxygen atoms) and Na4 (~nine-coordinated, see text for comments).
895 The bottom row includes polyhedra for mosandrite, the similar M4 and M5 sites (seven-
896 coordinated to six oxygen atoms and one OH^-) and the M3 site (coordinated to two oxygen and
897 six mixed anion sites). Red spheres are oxygen atoms, grey and green spheres are mixed anion
898 sites, and larger multicoloured spheres inside polyhedra are Ln^{3+}.

899 Figure 2. Imagery for Mt. Malosa zircon hand sample in (A) SWIR False Color, (B) SAM match
900 strength to input spectrum (located at crosshairs), (C) SWIR false color with overlapping ROIs
901 based on tightening SAM thresholds (ROI colors match spectra in Fig. 3), and (D) digital
902 photograph. The box in (D) is placed around a prominent cluster of zircon crystals.

903 Figure 3. Mean spectra in the SWIR of ROI based on different SAM thresholds, as labeled, for
904 illustrative purposes of generating an average spectrum. The top black spectrum is the input
905 spectrum from a single pixel, and the purple spectrum is the mean from pixels included when the
906 SAM threshold was set to >0.02, resulting in 40 pixels. Other spectra (color-coded to the
907 corresponding ROI) are from less-strict SAM thresholds as labeled, and therefore represent
908 larger ROIs.

909 Figure 4. Selected chondrite-normalized REE plots for eudialyte and mosandrite. Eudialyte
910 CMN72-24 (higher LREE) is from Mont Saint-Hilaire while hand sample F92-23 with both

eudialyte (higher HREE) and mosandrite originates from Kipawa. Missing points due to analytes being below detection.

Figure 5. Reflectance spectra of cerite in the VNIR (500 – 1000 nm) and SWIR (975 – 2530 nm) ranges. Clusters are indicated by labeled thick horizontal lines and prominent absorptions highlighted in the Index Table are labeled with wavelength position.

Figure 6. Reflectance spectra of mosandrite in the VNIR (500 – 1000 nm) and SWIR (975 – 2530 nm) ranges. Clusters are indicated by labeled thick horizontal lines and prominent absorptions highlighted in the Index Table are labeled with wavelength positions.

Figure 7. Reflectance spectra of kainosite in the VNIR (550 – 1000 nm) and SWIR (975 – 2530 nm) ranges. Clusters are indicated by labeled thick horizontal lines and prominent absorptions highlighted in the Index Table are labeled with wavelength positions.

Figure 8. Stacked reflectance spectra of zircon samples in the VNIR (550 – 1000 nm) and SWIR (975 – 2530 nm) ranges. Clusters are indicated by labeled thick horizontal lines and prominent absorptions highlighted in the Index Tables are labeled with wavelength positions. Uranium-related features are distinguished by lettered clusters, yellow horizontal bars, and italicized wavelength labels. From top down, Mt. Malosa (pink, MM), Green River (blue, GR), North Burgess (green, NB), Mudtank (red, MT), St. Peters Dome (black, SP).

Figure 9. Reflectance spectra of zircon samples in the VNIR (550 – 1000 nm) and SWIR (975 – 2530 nm) ranges. Clusters are indicated by labeled thick horizontal lines and prominent absorptions highlighted in the Index Tables are labeled with wavelength positions. Uranium-related features are distinguished by lettered clusters, yellow horizontal bars, and italicized wavelength labels. Color schemes remain for the unstacked spectra: Mt. Malosa (pink, MM),

933 Green River (blue, GR), North Burgess (green, NB), Mudtank (red, MT), St. Peters Dome
934 (black, SP).

935 Figure 10. Reflectance spectra of eudialyte samples in the VNIR (550 – 1000 nm) and SWIR
936 (975 – 2530 nm) ranges. Clusters are indicated by labeled thick horizontal lines, and prominent
937 absorptions for sample "Kipawa-Mariano" (black spectrum) are labeled with wavelength
938 positions.

939 Figure 11. Stacked reflectance spectra of eudialyte samples in the VNIR (550 – 1000 nm) and
940 SWIR (975 – 2530 nm) ranges. Clusters are indicated by labeled thick horizontal lines and
941 prominent absorptions highlighted in the Index Tables are labeled with wavelength positions.
942 The stacked VNIR spectra are ordered by LREE:HREE ratio; note that the samples above
943 CMNOC478 have HREE enrichment greater than 1. The stacked SWIR spectra are ordered by
944 the position of the reflectance maximum between 1050 and 1400 nm. Clusters are repeated for
945 the different groupings of samples.

946 Figure 12. Stacked reflectance spectra from representative REE-bearing silicate minerals in the
947 VNIR (500 to 1000 nm) and SWIR (975 - 2530 nm) ranges. Clusters as described in the text are
948 indicated by labeled thick horizontal lines with prominent absorptions identified by tick marks.
949 These are compiled at the bottom of the figure.

950 Figure 13. Selected samples showing the Er^{3+}-Yb^{3+} related absorption band near 978 nm. Spectra
951 are labeled with sample name and Er and Yb contents in parentheses (Er_2O_3 wt% / Yb_2O_3 wt%).

952 Figure 14. Reflectance spectra (left) of selected REE-bearing silicate minerals and their
953 continuum-removed spectra (right) displaying relative intensity and positional differences for
954 Nd^{3+}-related absorptions centered at ~746 nm ($^4I_{9/2} \rightarrow {}^4F_{7/2}+{}^4S_{3/2}$), ~803 nm ($^4I_{9/2} \rightarrow {}^4F_{5/2}+{}^2H_{9/2}$),

and 875 nm ($^4I_{9/2} \rightarrow {}^4F_{3/2}$). Influence from Dy^{3+} in these samples is minimal but would be greatest in the ~803 nm cluster. Weight% of Nd_2O_3 for each sample is given in parentheses.

958 **TABLES**

959 Table 1. Summary of REE site coordination polyhedra for the various REE-bearing silicate minerals.

	Zircon	Kainosite	Cerite	Eudialyte	Mosandrite
REE Site 1 Coordination	8	8	9	6 (*M*1)	7 (*M*4)
Distortion Index	0.032	0.044	0.037	0.015	0.040
Volume ($Å^3$)	19.13	23.62	33.71	15.53	20.30
Comments	Replaces Zr, 8×O	8×O	8×O, 1×OH	Ca>Mn>REE, 6×O	6×O, 1×OH
REE Site 2 Coordination			9	9 (*Na*4)	7 (*M*5)
Distortion Index			0.032	0.079	0.025
Volume ($Å^3$)			32.85	40.27	21.26
Comments			8×O, 1×OH	Can be six to 10 coordinated, variable anion bonding	6×O, 1×OH
REE Site 3 Coordination			9		6 (*M*3)
Distortion Index			0.051		0.023
Volume ($Å^3$)			34.64		16.22
Comments			8×O, 1×OH		4×Mixed Anion, 2×O

960 *Data for polyhedra from Rumanova et al. (1967), Johnsen and Grice (1999), Finch et al. (2001),
961 Pakhomovsky et al. (2002), and Bellezza et al. (2009). Distortion index based on Baur (1974) via
962 Momma and Izumi (2011)

963

964 Table 2. Pixel counts per sample used to produce average spectra in the VNIR and SWIR ranges.

Mineral	Sample	VNIR Pixels	SWIR Pixels
Cerite	Bastnas	9459	1853
Mosandrite	Kipawa CMN F92-23	2977	1228
Kainosite	Long Lake	175	22
Zircon	Green River	4391	497
	Mudtank	7424	2365
	North Burgess	12172	2110
	Mt. Malosa	701	40
	St. Peters Dome	948	195
Eudialyte	MSH CMN 72-24	9414	222
	MSH CMN 88-79 (Pinch Collection)	5890	476
	MSH CMNOC 2045	11171	730
	MSH CMNOC 37104	7141	2867
	MSH CMNOC 478	11324	986
	MSH CMNOC 476	5856	178
	Kipawa UofA Fragment	2416	227
	Kipawa Mariano	4070	3186
	Kipawa CMN F92-23	12305	1313

965

966

967 Table 3. Chemical variation relevant to reflectance spectroscopy, as well as probable ages and geological
968 settings for the zircon samples.

Sample	U and Th	REE	Analytical Total (wt%)	Age	Geological Setting	Reference
Mudtank	Below detection	Very Low	98.24	732 Ma	Carbonatite	Currie et al. (1992)
St. Peters Dome	Below detection	Low	96.04	~1 Ga	Pegmatites of A-type granite suite	Smith et al. (1999)
Mt. Malosa	Below detection	High	95.82	~113 Ma	Pegmatites of A-type granite suite	Eby et al. (1995, Guastoni et al. (2009)
North Burgess	Moderate	Very Low	98.63	1 Ga?	Pegmatite-related metasomatic skarn?	Currie (1951)
Green River	High	Moderate	98.37	329 Ma	Syenitic pegmatite	Braun et al. (2009)

969 *Analytical total is given as a rough proxy for degree of metamictization.

970

971 Table 4. Prominent absorption features of cerite in the VNIR and SWIR ranges.

Cerite	Cluster	Abs	Shape	Probable Origin
VNIR Range	1	523	MIN	Nd
	2	583	MIN - st	Nd, Pr
		627	SH - n	Nd
		642	SH - n	Nd
		661	SH - n	Nd
	3	681	MIN	Nd
	4	737	MIN	Nd
		746	MIN - st	Nd
		753	SH	Nd
	5	797	MIN	Nd
		803	MIN - st	Nd
		811	SH	Nd
		825	SH	Nd
	6	864	MIN - st	Nd
		876	MIN - st	Nd
		888	SH	Nd
		898	SH	Nd
		945	MIN - w, n	Sm
		961	MIN - w, n	Sm
SWIR Range	7	1010	SH	Pr
		1080	MIN - st	Sm
		1112	SH	Sm
	8	1232	MIN - st	Sm
		1263	SH	Sm
	9	1383	MIN	Sm
		1408	SH	H_2O / OH
		1452	MIN	Pr
		1540	MIN - st	Pr>Sm
		1578	SH	Pr, Sm Nd
		1622	SH	Pr, Sm Nd
		1710	MIN	Nd
	10	1968	MIN - st	Pr, Sm, H_2O
		2030	SH	Pr>Eu
	11	2193	MIN	OH/REE/Mg-Fe
	*	2243	MIN - w	OH/REE/Mg-Fe
	*	2312	MIN	OH/REE/Mg-Fe
	*	2330	MIN	OH/REE/Mg-Fe
		2355	SH	OH/REE/Mg-Fe
		2380	SH	OH/REE/Mg-Fe
		2424	MIN - st	OH/REE/Mg-Fe
		2487	MIN	OH/REE/Mg-Fe
		2518	SH	OH/REE/Mg-Fe

972 Note: Absorption bands marked with * share distinct wavelength positions with bastnaesite.

973

974

975 Table 5. Prominent absorption features of mosandrite in the VNIR and SWIR ranges.

Mosandrite	Cluster	Abs	Shape	Probable Origin
VNIR Range	1	527	MIN	Nd
		547	SH - n	Nd
	2	574	MIN - st	Nd, Pr
		586	MIN - st	Nd, Pr
		615	SH	Nd
		627	SH - n	Nd
		651	SH - b, n	Er
	3	681	MIN	Nd
	4	736	MIN	Nd
		740	MIN - st	Nd>Dy
		745	MIN	Nd > Dy
	5	772	SH	Nd > Dy
		795	SH	Nd > Dy
		804	MIN - st	Nd > Dy
		811	SH	Nd > Dy
	6	864	SH	Nd
		874	MIN - st	Nd
		880	SH	Nd
		919	SH - n	Dy
		945	MIN - w, n	Sm > Dy
	7	976	MIN - st	Er, Yb
SWIR Range	8	1074	MIN - st	Sm
		1093	SH	Sm
	9	1232	SH	Sm
		1257	MIN - st	Sm
	10	1377	SH	Sm
		1440	SH	H_2O / OH
		1471	MIN - st	Pr
		1528	MIN	Sm>Pr, Er
		1585	SH	Sm>Pr, Nd
	11	1729	SH	Nd, Dy
		1817	SH	Nd, Dy
		1930	MIN - st	H_2O
	12	2318	MIN	OH/REE/Ti
		2393	SH	OH/REE/Ti
		2418	SH	OH/REE/Ti
		2462	MIN	OH/REE/Ti

976

977

978

979

980 Table 6. Prominent absorption features of kainosite in the VNIR and SWIR ranges.

Kainosite	Cluster	Abs	Shape	Probable Origin
VNIR Range	1	576	MIN - n	Nd
		585	MIN - n	Nd
		596	SH - n	Nd
	2	651	MIN - n	Ho, Er
	3	737	MIN	Nd, Dy
		743	SH - n	Nd, Dy
		745	SH - n	Nd, Dy
		750	MIN - st	Nd, Dy
		754	MIN	Nd, Dy
	4	782	SH - n	Nd, Dy, Er
		795	MIN	Nd, Dy, Er
		805	MIN - st	Nd, Dy, Er
		814	MIN	Nd, Dy, Er
		820	SH	Nd, Dy, Er
	5	865	MIN	Nd
		876	MIN	Nd
		887	MIN - n	Nd, Ho, Dy
		896	MIN - n	Dy, Nd
	6	978	MIN	Er, Yb
SWIR Range	7	1080	MIN	Sm
		1105	SH	Dy, U?
		1156	SH	Dy, Ho
	8	1232	MIN	Dy, Sm
		1263	MIN	Dy, Sm
		1288	SH	Dy
	9	1377	MIN	Sm
	10	1415	SH	H_2O / OH
		1484	MIN - st	Er, Pr
		1528	MIN	Er>Sm
	11	1653	SH - w	Dy, Nd
		1723	MIN - w	Dy, Nd, Tb
	12	1961	MIN - st	H_2O, Eu, Pr, Ho
		2055	MIN - st	U?, Sm, Pr, Ho, Tb
		2105	SH	Sm, Pr, Ho
	13	2199	MIN - w	CO_3 / OH / REE
		2243	SH	CO_3 / OH / REE
		2268	SH	CO_3 / OH / REE
		2318	SH	CO_3 / OH / REE
		2387	MIN - st	CO_3 / OH / REE
		2474	MIN	CO_3 / OH / REE
		2505	SH	CO_3 / OH / REE

981

982

983

984

985 Table 7. Prominent absorption features of zircon samples in the VNIR range.

		Zircon	St Peters Dome		Mudtank		North Burgess		Green River		Mt Malosa	
Cluster	U		Abs	Shape	Abs	Shape	Abs	Shape	Abs	Shape	Abs	Shape
1		Nd									575	SH
		Nd									576	MIN
		Nd									582	MIN
		Nd							589	SH - w, n	585	SH
		Nd									594	MIN
2	A	U4+ and Er					653	MIN - w	654	MIN	651	MIN - n
		Er							661	SH	660	SH - n
		Nd							683	SH - w	681	MIN - n, w
	B	U4+					691	SH - w	690	MIN		
3		Nd>Dy							738	MIN - w	739	MIN - st
		Nd>Dy							750	MIN	750	MIN - st
		Nd							756	SH - w	757	MIN
		Nd							760	SH - w	769	SH
		Nd									774	SH
4		Nd>Er,Dy							781	MIN - w	781	MIN
		Nd>Er,Dy							797	SH	796	SH
		Nd>Er,Dy							803	MIN	802	SH
		Nd>Er,Dy							808	MIN - st	808	MIN - st
		Nd>Er,Dy									819	SH
		Er									835	MIN - n
		Er									844	MIN - n
	C	U4+?							849	MIN - b		
5		Nd									870	MIN - st
		Nd							882	SH	880	MIN - st
		Dy	892	MIN - w			892	MIN - w	894	MIN	893	MIN
	D	U4+			916	MIN - n, w	916	MIN - n, w	916	MIN - st	915	MIN - w
	E	U4+					961	MIN - n, w	961	SH - b		
6		Er, Yb							978	MIN - st	978	MIN

986 * REE related absorption clusters are labeled with numbers and shaded in grey, while U-related
987 absorptions are labeled with letters.

988

989

990 Table 8. Prominent absorption features of zircon samples in the SWIR range.

		Zircon	St Peters Dome		Mudtank		North Burgess		Green River		Mt Malosa	
Cluster	U		Abs	Shape	Abs	Shape	Abs	Shape	Abs	Shape	Abs	Shape
	F	U4+	1010	SH - w	1010	SH	1010	MIN - w	1010	SH		
	F	U4+	1061	SH - w	1055	SH	1055	MIN	1061	MIN		
7		Sm	1086	SH - w							1086	MIN
		Sm									1105	MIN
	G	U5+	1118	SH - w	1112	MIN	1112	MIN	1118	MIN	1112	SH
	G	U4+	1137	SH - w	1149	SH	1149	SH	1143	SH - w	1143	SH
8		Sm?									1200	SH
		Sm									1244	MIN
		Sm, Dy							1263	SH	1263	MIN
		Dy							1288	MIN - w	1288	SH
	H	U4+			1326	MIN	1326	MIN	1326	MIN		
	H	U4+			1345	MIN - w	1345	SH	1345	SH	1332	SH
9		Sm							1389	SH	1389	MIN
		H_2O / OH	1415	MIN					1415	MIN - w	1415	MIN - w
10	I	U4+, Er	1478	MIN - w	1478	SH	1478	SH	1478	SH	1427	SH - w
	I	U5+	1503	MIN - w	1503	MIN - st	1503	MIN - st	1503	MIN - st	1503	MIN - st
	I	U4+, Er, Sm	1522	SH - w	1534	SH	1534	SH	1534	SH	1528	SH
		Er, Sm									1560	MIN
		Sm	1616	SH - w							1616	MIN - w
	J	U4+	1654	MIN - w	1660	MIN	1660	MIN	1660	MIN	1660	MIN
11		Dy									1691	MIN - w
	J	U4+			1704	MIN	1704	MIN	1704	MIN - w		
		Nd?	1729	MIN - w, b	1742	SH - w	1742	SH - w	1729	MIN - w, b	1729	MIN
	K	U4+			1792	SH - w	1792	SH - w	1792	SH - w		
12		H_2O	1924	MIN - st	1924	SH	1917	MIN - b	1930	MIN	1917	SH
		Sm									1943	MIN
	L	U4+	2068	MIN - w	2068	MIN - st	2068	MIN - st	2074	MIN - st	2074	SH - w
	M	U4+			2187	SH	2187	SH				
13		Comb & Overt	2206	MIN - st	2206	SH			2206	MIN		
		Comb & Overt	2256	SH	2268	MIN - w	2262	SH	2262	SH		
		Comb & Overt	2312	SH	2306	SH	2306	MIN	2305	MIN	2312	MIN
		Comb & Overt	2355	MIN	2362	SH	2349	SH	2355	MIN	2349	MIN
		Comb & Overt	2387	MIN			2393	SH	2393	MIN	2474	MIN
		Comb & Overt	2443	SH	2462	MIN						
		Comb & Overt	2499	MIN							2499	MIN
		Comb &	2511	MIN - w								

* REE related absorption clusters are labeled with numbers and shaded in grey, while U-related absorptions are labeled with letters.

995 Table 9. Prominent absorption features of HREE-enriched eudialyte samples in the VNIR and SWIR
996 ranges.

Eudialyte	Kipawa-Mariano		Kipawa - UofA		Kipawa F92-23		CMNOC 478		Probable Origin
LREE/HREE	0.4		0.4		0.5		2.7		
Cluster	Abs	Shape	Abs	Shape	Abs	Shape	Abs	Shape	
1					576	SH - n	576	MIN - n	Nd
					584	SH - n	584	MIN - n	Nd
2	651	MIN - w	651	MIN - w	651	MIN - w			Er, U?
	661	MIN - w, n	661	MIN - w, n	661	MIN - w, n			Er
	680	SH	680	SH	680	SH			Er
3	733	SH	735	MIN	734	MIN	735	MIN - w	Dy, Nd
	741	MIN - st	745	MIN - st	745	MIN - st	745	MIN - w	Dy, Nd
	750	MIN	752	MIN	752	MIN	754	MIN - w	Dy, Nd
	760	SH							Dy
4	800	MIN - st	800	MIN - st	800	MIN - st	800	MIN	Nd, Dy, Er
	808	MIN	809	SH	809	SH	804	MIN - w	Nd, Dy, Er
	824	SH							Nd, Dy, Er
5	865	SH	865	SH	865	SH	865	SH - w	Nd, Dy
	873	MIN	872	MIN	872	MIN	872	SH - w	Nd, Dy
	880	MIN							Nd, Dy
	888	SH - b	888	SH - b	888	SH - b			Dy
	910	MIN	910	MIN - b	910	MIN - b			Dy
6	974	MIN - st	974	MIN	975	MIN			Er, Yb
$^{V}Fe^{2+}$	-	-	914	MIN - b	914	MIN - b	914	MIN - b	$^{V}Fe^{2+}$
7	1061	MIN	1067	SH	1067	SH			Dy, Sm, U?
	1099	SH	1105	SH - w					Dy
8	1168	SH	1168	SH	1168	SH			Dy, U?
	1213	SH	1213	SH	1213	SH	1200	SH - w	Dy, Sm
	1276	MIN	1276	MIN	1276	MIN	1263	SH	Dy, Sm
	1358	SH	1358	SH	1358	SH			Dy, U4+?
	1408	MIN	1408	MIN	1408	MIN			H_2O / OH, Sm
	1433	MIN - st	1440	MIN - st	1433	MIN - st	1433	MIN - st	H_2O / OH
	1478	SH	1478	SH	1478	SH	1471	MIN	Pr, Er, U4+?
	1534	MIN	1534	MIN	1534	MIN	1540	SH	Er, Sm, U4+?
	1566	SH - w	1566	SH - w	1566	SH - w			Er
9									Nd
	1811	SH	1811	SH	1811	SH	1792	SH	U4+?
	1930	MIN - st	1930	MIN - st	1930	MIN - st	1924	MIN - st	Pr, Sm, H_2O
			2074	SH - w, b	2093	SH - w, b	2080	SH - w, b	U4+?
10	2193	SH	2193	SH	2193	SH	2193	SH	OH/REE/Mn-Fe
									OH/REE/Mn-Fe
									OH/REE/Mn-Fe

	2312	SH	2312	SH	2318	MIN - w	2312	MIN - w	OH/REE/Mn-Fe
	2437	MIN	2443	MIN	2437	MIN	2437	SH	OH/REE/Mn-Fe
	2493	SH	2493	SH	2493	SH	2474	MIN	OH/REE/Mn-Fe
Refl. Peak	1118		1156		1143		1320		

997

998

999 Table 10. Prominent absorption features of LREE-enriched eudialyte samples in the VNIR and SWIR
1000 ranges.

Eudialyte	CMNOC 2045		CMNOC 476		CMN 88-79 Pinch		CMN 72-24		CMNOC 37104		Probable
LREE/HREE	4.6		6.2		8.5		9.5		10.6		Origin
Cluster	Abs	Shape	Abs	Shape	Abs	Shape	Abs	Shape	Abs	Shape	
1	576	MIN - n, w									Nd
					582	MIN - w, n	581	MIN - w, n	593	SH - n	Nd
2					656	MIN - w, n					Er, U?
											Er
											Er
3					735	SH					Dy, Nd
	737	SH - v w	739	MIN - st	740	MIN - st	740	MIN	740	MIN	Dy, Nd
	753	SH - v w	751	MIN	752	MIN	750	MIN	751	MIN	Dy, Nd
											Dy
4			801	MIN	798	SH - n	796	MIN	795	MIN	Nd, Dy, Er
			810	MIN - st	807	MIN - st	808	MIN	807	MIN	Nd, Dy, Er
			826	SH			824	SH - n			Nd, Dy, Er
5			869	SH	866	MIN	864	MIN	863	MIN	Nd, Dy
											Nd, Dy
			880	MIN	880	MIN	880	MIN	879	MIN	Nd, Dy
											Dy
											Dy
6											Er, Yb
$^{V}Fe^{2+}$	920	MIN - b	916	MIN - b	886	MIN - b	-	-	-	-	$^{V}Fe^{2+}$
7			1061	SH - w	1061	SH - w	1061	SH - w	1061	SH - w	Dy, Sm, U?
											Dy
8			1162	SH	1162	SH	1162	SH	1162	SH	Dy, U?
	1200	SH - w	1213	MIN - w	1206	MIN - w	1200	SH	1200	SH	Dy, Sm
			1269	SH	1263	SH	1251	SH	1251	SH	Dy, Sm
	1351	SH - w	1351	SH	1351	SH	1351	SH	1351	SH	Dy, U4+?
	1408	SH	1408	SH	1408	SH					H_2O / OH, Sm
	1440	MIN	1440	MIN - st	1440	MIN - st	1427	MIN - st	1433	MIN - st	H_2O / OH
	1478	MIN - w	1478	SH -w	1478	SH	1478	SH	1478	SH	Pr, Er, U4+?
					1553	SH					Er, Sm, U4+?
											Er
9					1729	SH					Nd
			1817	SH	1817	SH	1805	SH	1805	SH	U4+?
	1936	MIN - st	1930	MIN - st	1930	MIN - st	1930	MIN - st	1930	MIN - st	Pr, Sm, H_2O
	2087	MIN - w, b	2093	SH - w, b	2087	SH - b					U4+?
10	2193	MIN - w, b			2193	SH					OH/REE/Mn-Fe
	2230	MIN - w			2237	SH	2249	MIN - st	2256	MIN - st	OH/REE/Mn-Fe
	2274	SH - w	2268	SH	2274	MIN - w					OH/REE/Mn-Fe

	2324	MIN - w	2312	SH	2312	MIN	2312	MIN - w	2305	SH -w	OH/REE/Mn-Fe
					2349	SH	2330	SH - w			OH/REE/Mn-Fe
			2437	MIN - st	2443	MIN - st					OH/REE/Mn-Fe
			2462	MIN							OH/REE/Mn-Fe
			2487	SH	2487	SH	2480	MIN - st	2480	MIN - st	OH/REE/Mn-Fe
Refl. Peak	1307		1232		1307		1307		1307		

1005 Table 11. Cation site parameters for Yb^{3+} in REE-bearing silicate minerals.

	Kainosite	Zircon	Mosandrite		Eudialyte	
Cation Site	*Y*	*Zr*	*M*4, *M*5	*M*3	*M*1	*Na*4
Normal Occupant	Y≈HREE	Zr	Ca≈Ce	Na	Ca	Na
Normal Valence Charge	+3	+4	~+2.5	+1	+2	+1
Coordination #	8 (VIII)	8 (VIII)	7 (VII)	6 (VI)	6 (VI)	9 (IX)
Ionic Radius (Å)	~1.002	0.84	~1.065	1.02	1.00	1.24
Coordinated Anions	8×O	8×O	6×O, 1×OH	2×O, 4×Mixed	6×O	"Cavity"
Yb^{3+} Substitution						
Valence Charge	+3	+3	+3	+3	+3	+3
Ionic Radius (Å)	0.985	0.985	0.925	0.868	0.868	1.042
Charge Imbalance (Yb^{3+} - M^{X+})	0	-1	+0.5	+2	+1	+2
Yb^{3+} radius / M^{X+} Radius	0.98	1.17	0.87	0.85	0.87	0.84

1006 *Ionic radii from Shannon (1976)

1007

1008

1009 Appendix A. Electron microprobe compositions for mosandrite, cerite, and kainosite.

Sample	CMN F92-23	Bastnas	Long Lake		CMN F92-23	Bastnas	Long Lake
Mineral	Mosandrite	Cerite	Kainosite		Mosandrite	Cerite	Kainosite
# Analyses	*5*	*4*	*5*				
Nb_2O_5 (wt.%)	1.61	0.06	0.03	Nb^{5+} (apfu)	0.10	0.01	0.00
Ta_2O_5	0.05	0.00	0.00	Ta^{5+}	0.00	0.00	0.00
P_2O_5	0.02	0.01	0.05	P^{5+}	0.00	0.00	0.01
SiO_2	29.76	21.20	34.45	Si^{4+}	4.00	6.81	4.07
TiO_2	8.29	0.00	0.00	Ti^{4+}	0.84	0.00	0.00
ZrO_2	0.44	0.00	0.01	Zr^{4+}	0.03	0.00	0.00
UO_2	0.00	0.00	0.00	U^{4+}	0.00	0.00	0.00
ThO_2	0.10	0.00	0.00	Th^{4+}	0.00	0.00	0.00
Al_2O_3	0.06	0.01	0.00	Al^{3+}	0.01	0.00	0.00
La_2O_3	1.47	13.78	0.00	La^{3+}	0.07	1.63	0.00
Ce_2O_3	4.02	32.69	0.51	Ce^{3+}	0.20	3.84	0.02
Pr_2O_3	0.54	4.23	0.17	Pr^{3+}	0.03	0.50	0.01
Nd_2O_3	2.51	14.74	2.49	Nd^{3+}	0.12	1.69	0.11
Sm_2O_3	0.74	1.94	2.48	Sm^{3+}	0.03	0.22	0.10
Eu_2O_3	0.09	0.07	0.22	Eu^{3+}	0.00	0.01	0.01
Gd_2O_3	0.82	0.77	3.44	Gd^{3+}	0.04	0.08	0.14
Tb_2O_3	0.14	0.00	0.45	Tb^{3+}	0.01	0.00	0.02
Dy_2O_3	1.05	0.08	3.38	Dy^{3+}	0.05	0.01	0.13
Ho_2O_3	0.21	0.00	0.51	Ho^{3+}	0.01	0.00	0.02
Er_2O_3	0.57	0.00	1.56	Er^{3+}	0.02	0.00	0.06
Tm_2O_3	0.05	0.00	0.11	Tm^{3+}	0.00	0.00	0.00
Yb_2O_3	0.32	0.00	1.55	Yb^{3+}	0.01	0.00	0.06
Lu_2O_3	0.00	0.00	0.09	Lu^{3+}	0.00	0.00	0.00
Y_2O_3	5.96	0.91	19.97	Y^{3+}	0.43	0.16	1.26
SrO	0.09	0.00	0.00	Sr^{2+}	0.01	0.00	0.00
MgO	0.03	1.46	0.00	Mg^{2+}	0.01	0.70	0.00
FeO	0.05	1.00	0.00	Fe^{2+}	0.01	0.27	0.00
MnO	0.05	0.06	0.00	Mn^{2+}	0.01	0.02	0.00
CaO	26.68	1.94	15.50	Ca^{2+}	3.84	0.67	1.96
Na_2O	6.39	0.00	0.00	Na^{+}	1.67	0.00	0.00
Cl	0.02	0.08	0.00	Cl^{-}	0.01	0.04	0.00
F	4.63	1.00	0.00	F^{-}	1.97	1.02	0.00
H_2O*	4.49	2.77	2.54	H^{+}	4.03	5.94	2.00
CO_2*			6.20	C^{4+}	*NA*	*NA*	1.00
O=CL	0.00	-0.02	0.00	O^{2-}	17.26	29.94	16.00
O=F	-1.95	-0.42	0.00				

TOTAL	99.30	98.36	95.71
REE_2O_3	18.49	69.21	36.93

*H_2O and CO_2 determined by stoichiometry and formulae calculations can be found in text. K and Ba were sought but not detected.

1015 Appendix B. Electron microprobe compositions for zircon.

Sample	Green River	Mudtank	North Burgess	Mt Malosa	St Peters Dome		Green River	Mudtank	North Burgess	Mt Malosa	St Peters Dome
# Analyses	*7*	*5*	*5*	*5*	*5*						
Nb_2O_5 (wt.%)	0.18	0.16	0.18	1.53	0.19	Nb^{5+} (apfu)	0.00	0.00	0.00	0.02	0.00
P_2O_5	0.04	0.04	0.04	0.24	0.10	P^{5+}	0.00	0.00	0.00	0.01	0.00
SiO_2	31.93	32.11	32.21	30.65	31.70	Si^{4+}	1.00	1.00	1.00	0.99	1.01
TiO_2	0.00	0.00	0.00	0.03	0.00	Ti^{4+}	0.00	0.00	0.00	0.00	0.00
ZrO_2	65.10	65.69	65.95	58.01	63.70	Zr^{4+}	0.99	1.00	1.00	0.92	0.98
UO_2	0.08	0.00	0.02	0.00	0.00	U^{4+}	0.00	0.00	0.00	0.00	0.00
ThO_2	0.56	0.02	0.00	0.29	0.03	Th^{4+}	0.00	0.00	0.00	0.00	0.00
Al_2O_3	0.00	0.00	0.00	0.00	0.00	Al^{3+}	0.00	0.00	0.00	0.00	0.00
La_2O_3	0.00	0.00	0.01	0.02	0.00	La^{3+}	0.00	0.00	0.00	0.00	0.00
Ce_2O_3	0.01	0.00	0.00	0.24	0.00	Ce^{3+}	0.00	0.00	0.00	0.00	0.00
Pr_2O_3	0.00	0.00	0.01	0.05	0.00	Pr^{3+}	0.00	0.00	0.00	0.00	0.00
Nd_2O_3	0.00	0.00	0.00	0.48	0.00	Nd^{3+}	0.00	0.00	0.00	0.01	0.00
Sm_2O_3	0.00	0.00	0.00	0.42	0.00	Sm^{3+}	0.00	0.00	0.00	0.01	0.00
Eu_2O_3	0.01	0.00	0.00	0.04	0.00	Eu^{3+}	0.00	0.00	0.00	0.00	0.00
Gd_2O_3	0.00	0.00	0.00	0.37	0.00	Gd^{3+}	0.00	0.00	0.00	0.00	0.00
Tb_2O_3	0.00	0.00	0.00	0.00	0.00	Tb^{3+}	0.00	0.00	0.00	0.00	0.00
Dy_2O_3	0.01	0.00	0.01	0.29	0.01	Dy^{3+}	0.00	0.00	0.00	0.00	0.00
Ho_2O_3	0.00	0.00	0.00	0.05	0.01	Ho^{3+}	0.00	0.00	0.00	0.00	0.00
Er_2O_3	0.01	0.00	0.00	0.16	0.01	Er^{3+}	0.00	0.00	0.00	0.00	0.00
Tm_2O_3	0.00	0.01	0.00	0.02	0.00	Tm^{3+}	0.00	0.00	0.00	0.00	0.00
Yb_2O_3	0.00	0.01	0.00	0.30	0.04	Yb^{3+}	0.00	0.00	0.00	0.00	0.00
Lu_2O_3	0.01	0.00	0.00	0.00	0.00	Lu^{3+}	0.00	0.00	0.00	0.00	0.00
Y_2O_3	0.27	0.02	0.01	2.39	0.03	Y^{3+}	0.00	0.00	0.00	0.04	0.00
SrO	0.15	0.15	0.15	0.12	0.13	Sr^{2+}	0.00	0.00	0.00	0.00	0.00
MgO	0.00	0.00	0.00	0.00	0.01	Mg^{2+}	0.00	0.00	0.00	0.00	0.00
FeO	0.00	0.00	0.00	0.03	0.00	Fe^{2+}	0.00	0.00	0.00	0.00	0.00
MnO	0.00	0.01	0.01	0.05	0.02	Mn^{2+}	0.00	0.00	0.00	0.00	0.00
Na_2O	0.00	0.00	0.00	0.01	0.00	Na^{+}	0.00	0.00	0.00	0.00	0.00
Cl	0.00	0.00	0.00	0.00	0.01	Cl^{-}	0.00	0.00	0.00	0.00	0.00
F	0.01	0.03	0.05	0.04	0.03	F^{-}	0.00	0.00	0.01	0.00	0.00
O=CL	0.00	0.00	0.00	0.00	0.00	O^{2-}	4.00	4.00	4.00	4.00	4.00
O=F	0.00	-0.01	-0.02	-0.02	-0.01						
TOTAL	98.37	98.24	98.63	95.82	96.04						
REE_2O_3	0.32	0.04	0.04	4.83	0.10						

1016

1017 *Formula contents on the basis of four anions pfu. Ta, Ca, K, and Ba were sought but not detected.

Appendix C. Electron microprobe compositions for eudialyte samples (LREE group).

Sample	CMNOC 2045	CMNOC 476	CMN 88-79	CMN 72-24	CMNOC 37104		CMNOC 2045	CMNOC 476	CMN 88-79	CMN 72-24	CMNOC 37104
# *Analyses*	5	8	5	5	5						
Nb_2O_5 (wt.%)	1.80	1.95	2.24	2.48	1.96	Nb^{5+} (apfu)	0.43	0.43	0.51	0.56	0.43
Ta_2O_5	0.14	0.03	0.01	0.00	0.00	Ta^{5+}	0.02	0.00	0.00	0.00	0.00
P_2O_5	0.02	0.02	0.00	0.01	0.01	P^{5+}	0.01	0.01	0.00	0.00	0.00
SiO_2	48.03	51.97	49.98	51.31	53.21	Si^{4+}	25.60	25.57	25.34	25.57	25.67
TiO_2	0.03	0.07	0.10	0.32	0.29	Ti^{4+}	0.01	0.03	0.04	0.12	0.11
ZrO_2	10.86	11.96	12.27	11.19	11.73	Zr^{4+}	2.82	2.87	3.03	2.72	2.76
UO_2	0.00	0.00	0.00	0.03	0.07	U^{4+}	0.00	0.00	0.00	0.00	0.01
ThO_2	0.05	0.03	0.14	0.11	0.09	Th^{4+}	0.01	0.00	0.02	0.01	0.01
Al_2O_3	0.17	0.17	0.13	0.06	0.06	Al^{3+}	0.11	0.10	0.08	0.04	0.03
La_2O_3	1.16	0.76	1.48	1.01	1.05	La^{3+}	0.23	0.14	0.28	0.19	0.19
Ce_2O_3	2.04	1.32	2.93	1.93	1.88	Ce^{3+}	0.40	0.24	0.54	0.35	0.33
Pr_2O_3	0.19	0.12	0.30	0.17	0.15	Pr^{3+}	0.04	0.02	0.06	0.03	0.03
Nd_2O_3	0.58	0.39	0.92	0.59	0.52	Nd^{3+}	0.11	0.07	0.17	0.11	0.09
Sm_2O_3	0.10	0.06	0.16	0.08	0.07	Sm^{3+}	0.02	0.01	0.03	0.01	0.01
Eu_2O_3	0.01	0.00	0.00	0.00	0.00	Eu^{3+}	0.00	0.00	0.00	0.00	0.00
Gd_2O_3	0.07	0.05	0.12	0.05	0.05	Gd^{3+}	0.01	0.01	0.02	0.01	0.01
Tb_2O_3	0.02	0.00	0.00	0.00	0.00	Tb^{3+}	0.00	0.00	0.00	0.00	0.00
Dy_2O_3	0.20	0.05	0.04	0.02	0.00	Dy^{3+}	0.03	0.01	0.01	0.00	0.00
Ho_2O_3	0.02	0.01	0.01	0.01	0.00	Ho^{3+}	0.00	0.00	0.00	0.00	0.00
Er_2O_3	0.08	0.02	0.02	0.01	0.01	Er^{3+}	0.01	0.00	0.00	0.00	0.00
Tm_2O_3	0.00	0.00	0.00	0.00	0.00	Tm^{3+}	0.00	0.00	0.00	0.00	0.00
Yb_2O_3	0.04	0.01	0.01	0.01	0.00	Yb^{3+}	0.01	0.00	0.00	0.00	0.00
Lu_2O_3	0.00	0.00	0.00	0.00	0.00	Lu^{3+}	0.00	0.00	0.00	0.00	0.00
Y_2O_3	0.55	0.35	0.62	0.35	0.34	Y^{3+}	0.16	0.09	0.17	0.09	0.09
SrO	0.08	0.27	0.29	0.32	0.26	Sr^{2+}	0.03	0.08	0.09	0.09	0.07
MgO	0.00	0.03	0.03	0.02	0.02	Mg^{2+}	0.00	0.02	0.02	0.02	0.01
FeO	6.55	3.88	2.93	2.62	2.47	Fe^{2+}	2.92	1.60	1.24	1.09	1.00
MnO	2.67	3.87	7.90	9.14	8.60	Mn^{2+}	1.21	1.61	3.39	3.86	3.52
BaO	0.01	0.03	0.01	0.02	0.06	Ba^{2+}	0.00	0.01	0.00	0.00	0.01
CaO	7.95	9.20	3.78	5.53	5.75	Ca^{2+}	4.54	4.85	2.05	2.95	2.97
Na_2O	11.79	7.63	6.21	5.73	4.46	Na^{+}	12.19	7.28	6.10	5.54	4.17
K_2O	0.38	0.42	0.36	0.30	0.18	K^{+}	0.26	0.26	0.23	0.19	0.11
Cl	1.03	0.79	0.53	0.39	0.45	Cl^{-}	0.93	0.66	0.46	0.33	0.37
F	0.18	0.09	0.19	0.18	0.08	F^{-}	0.30	0.14	0.31	0.28	0.12
H_2O*	1.06	1.28	1.25	1.32	1.40	H^{+}	3.77	4.20	4.24	4.39	4.51
O=CL	-0.23	-0.18	-0.12	-0.09	-0.10	O^{2-}	75.93	72.72	71.86	72.26	71.09
O=F	-0.08	-0.04	-0.08	-0.08	-0.03						
TOTAL	97.55	96.61	94.76	95.15	95.09						
REE_2O_3	5.06	3.14	6.61	4.23	4.07						
L / H	4.56	6.14	8.44	9.58	10.63						

*H_2O determined by stoichiometry based on five apfu at the two X sites. Formula contents based on 29 apfu at the Zr and Si(7) sites (Si, Al, Zr, Ti, Nb, Ta).

1024 Appendix D. Electron microprobe compositions for eudialyte samples (HREE group).

Sample	Kipawa-M	Kipawa-UofA	CMN F92-23	CMNOC 478		Kipawa-M	Kipawa-UofA	CMN F92-23	CMNOC 478
# *Analyses*	11	5	5	15					
Nb_2O_5 (wt.%)	0.73	0.97	0.77	3.19	Nb^{5+} (apfu)	0.18	0.22	0.18	0.80
Ta_2O_5	0.01	0.08	0.05	0.00	Ta^{5+}	0.00	0.01	0.01	0.00
P_2O_5	0.00	0.00	0.02	0.02	P^{5+}	0.00	0.00	0.01	0.01
SiO_2	47.58	51.30	50.90	45.54	Si^{4+}	25.32	25.63	25.81	25.28
TiO_2	0.35	0.30	0.29	0.10	Ti^{4+}	0.14	0.11	0.11	0.04
ZrO_2	12.75	12.21	11.48	10.44	Zr^{4+}	3.31	2.97	2.84	2.83
UO_2	0.00	0.02	0.00	0.00	U^{4+}	0.00	0.00	0.00	0.00
ThO_2	0.01	0.00	0.04	0.08	Th^{4+}	0.00	0.00	0.01	0.01
Al_2O_3	0.09	0.10	0.10	0.08	Al^{3+}	0.06	0.06	0.06	0.05
La_2O_3	0.33	0.38	0.42	1.28	La^{3+}	0.07	0.07	0.08	0.26
Ce_2O_3	0.56	0.61	0.65	2.45	Ce^{3+}	0.11	0.11	0.12	0.50
Pr_2O_3	0.05	0.05	0.04	0.22	Pr^{3+}	0.01	0.01	0.01	0.04
Nd_2O_3	0.24	0.25	0.22	0.60	Nd^{3+}	0.05	0.05	0.04	0.12
Sm_2O_3	0.12	0.06	0.07	0.10	Sm^{3+}	0.02	0.01	0.01	0.02
Eu_2O_3	0.00	0.02	0.01	0.01	Eu^{3+}	0.00	0.00	0.00	0.00
Gd_2O_3	0.15	0.08	0.08	0.08	Gd^{3+}	0.03	0.01	0.01	0.02
Tb_2O_3	0.04	0.00	0.04	0.03	Tb^{3+}	0.01	0.00	0.01	0.01
Dy_2O_3	0.49	0.40	0.27	0.32	Dy^{3+}	0.08	0.06	0.04	0.06
Ho_2O_3	0.05	0.09	0.09	0.04	Ho^{3+}	0.01	0.01	0.02	0.01
Er_2O_3	0.48	0.30	0.29	0.14	Er^{3+}	0.08	0.05	0.05	0.02
Tm_2O_3	0.01	0.04	0.03	0.01	Tm^{3+}	0.00	0.01	0.01	0.00
Yb_2O_3	0.41	0.40	0.36	0.20	Yb^{3+}	0.07	0.06	0.06	0.03
Lu_2O_3	0.02	0.03	0.02	0.00	Lu^{3+}	0.00	0.01	0.00	0.00
Y_2O_3	2.67	2.54	2.11	0.99	Y^{3+}	0.76	0.68	0.57	0.29
SrO	0.19	0.18	0.22	0.12	Sr^{2+}	0.06	0.05	0.07	0.04
MgO	0.09	0.10	0.10	0.01	Mg^{2+}	0.07	0.07	0.08	0.01
FeO	2.44	2.28	2.68	3.18	Fe^{2+}	1.09	0.95	1.14	1.48
MnO	1.33	1.37	1.46	6.68	Mn^{2+}	0.60	0.58	0.63	3.14
BaO	0.09	0.21	0.15	0.01	Ba^{2+}	0.02	0.04	0.03	0.00
CaO	11.91	12.44	12.71	8.49	Ca^{2+}	6.79	6.66	6.91	5.05
Na_2O	4.11	10.46	11.08	11.12	Na^{+}	4.24	10.13	10.89	11.97
K_2O	0.57	0.49	0.51	0.29	K^{+}	0.39	0.31	0.33	0.21
Cl	1.08	1.13	1.20	0.92	Cl^{-}	0.97	0.96	1.03	0.87
F	0.17	0.12	0.16	0.13	F^{-}	0.29	0.19	0.26	0.23
H_2O*	1.05	1.16	1.10	1.05	H^{+}	3.74	3.85	3.71	3.91
O=CL	-0.24	-0.25	-0.27	-0.21	O^{2-}	72.17	74.73	75.28	77.70
O=F	-0.07	-0.05	-0.07	-0.05					
TOTAL	89.86	99.86	99.38	97.66					
REE_2O_3	5.62	5.25	4.70	6.47					

L / H	0.35	0.38	0.46	2.74

*H_2O determined by stoichiometry based on five apfu at the two X sites. Formula contents based on 29 apfu at the Zr and Si(7) sites (Si, Al, Zr, Ti, Nb, Ta).

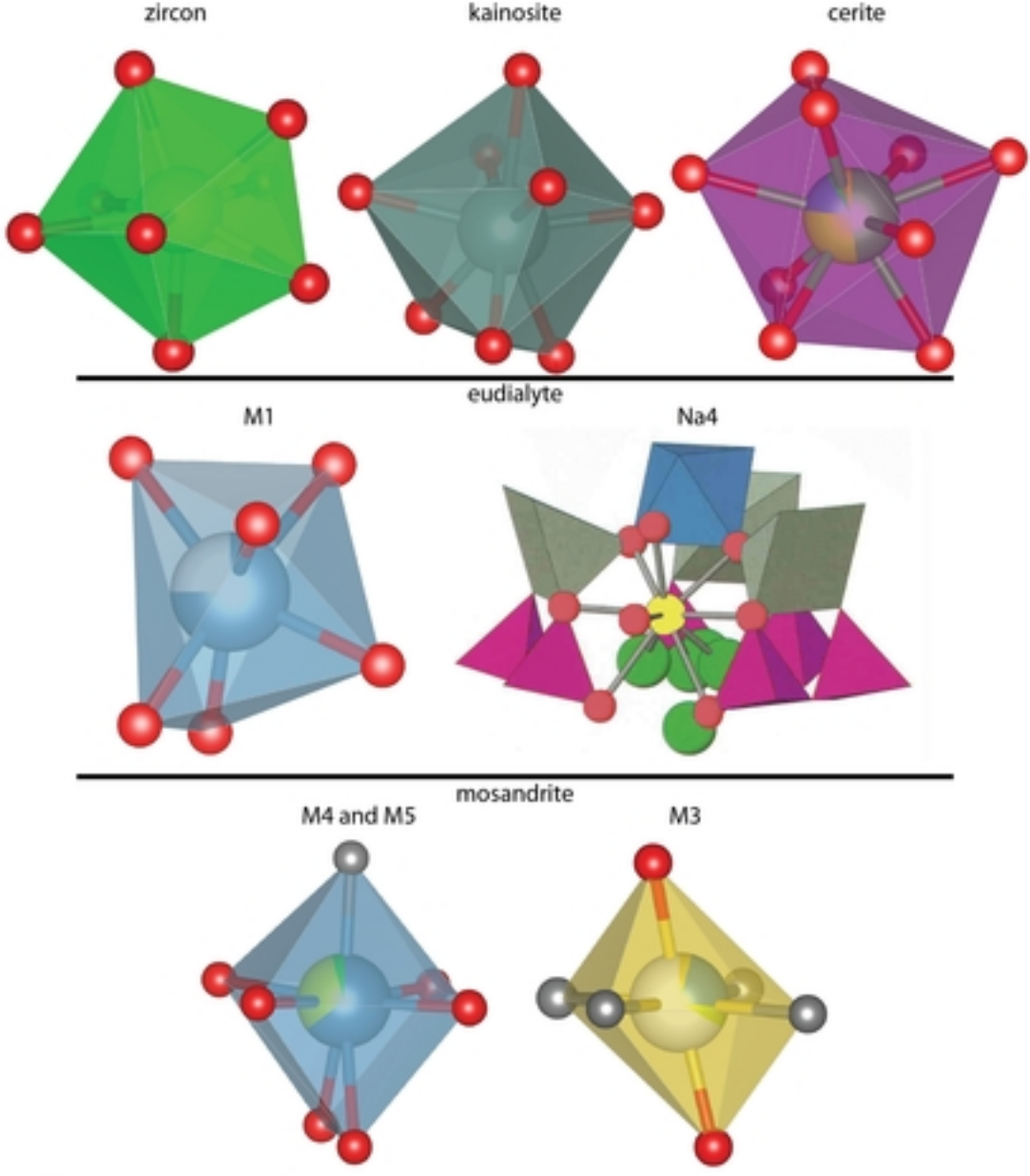
zircon
kainosite
cerite
eudialyte
M1
Na4
mosandrite
M4 and M5
M3

Figure 1

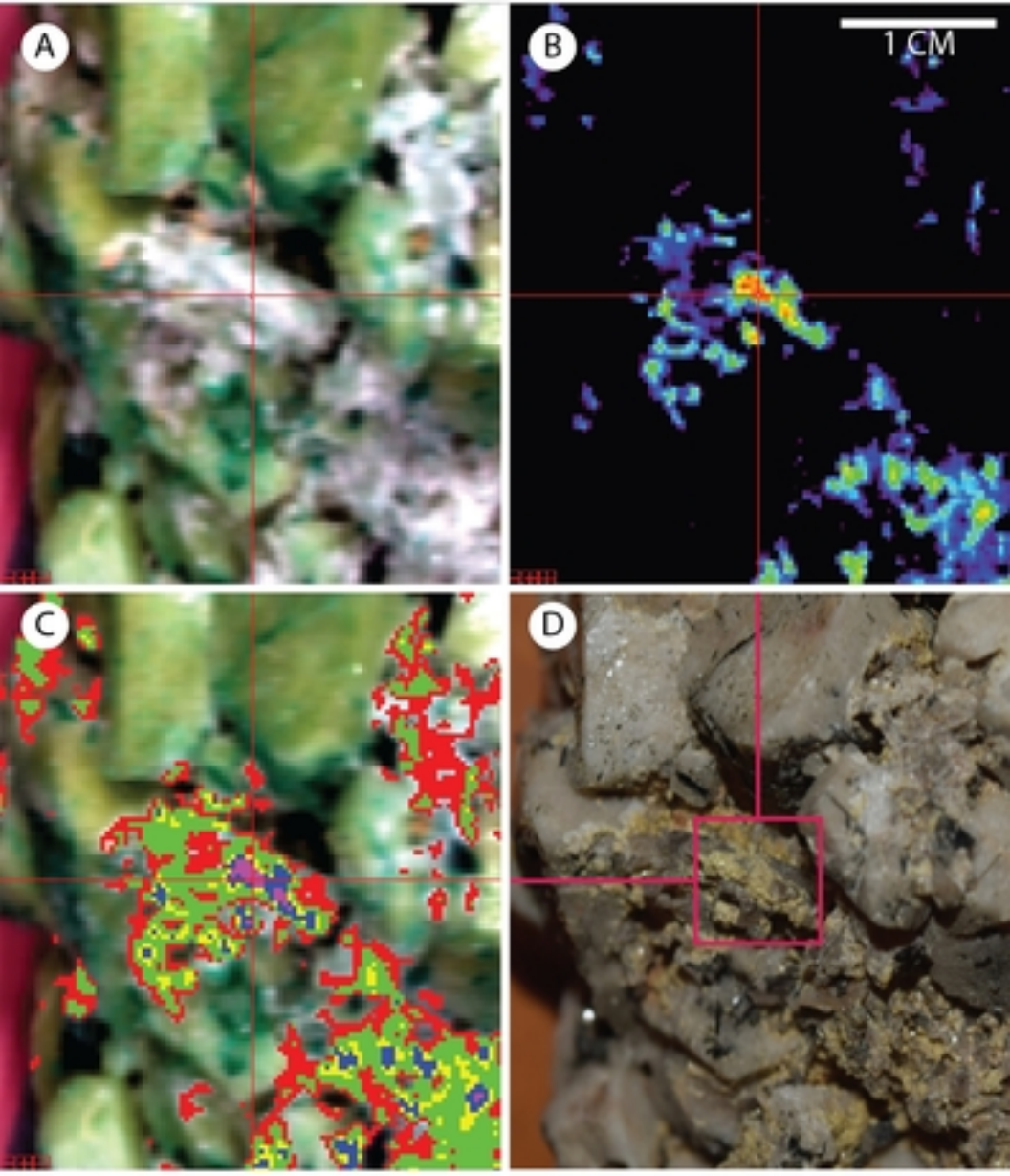

Figure 2

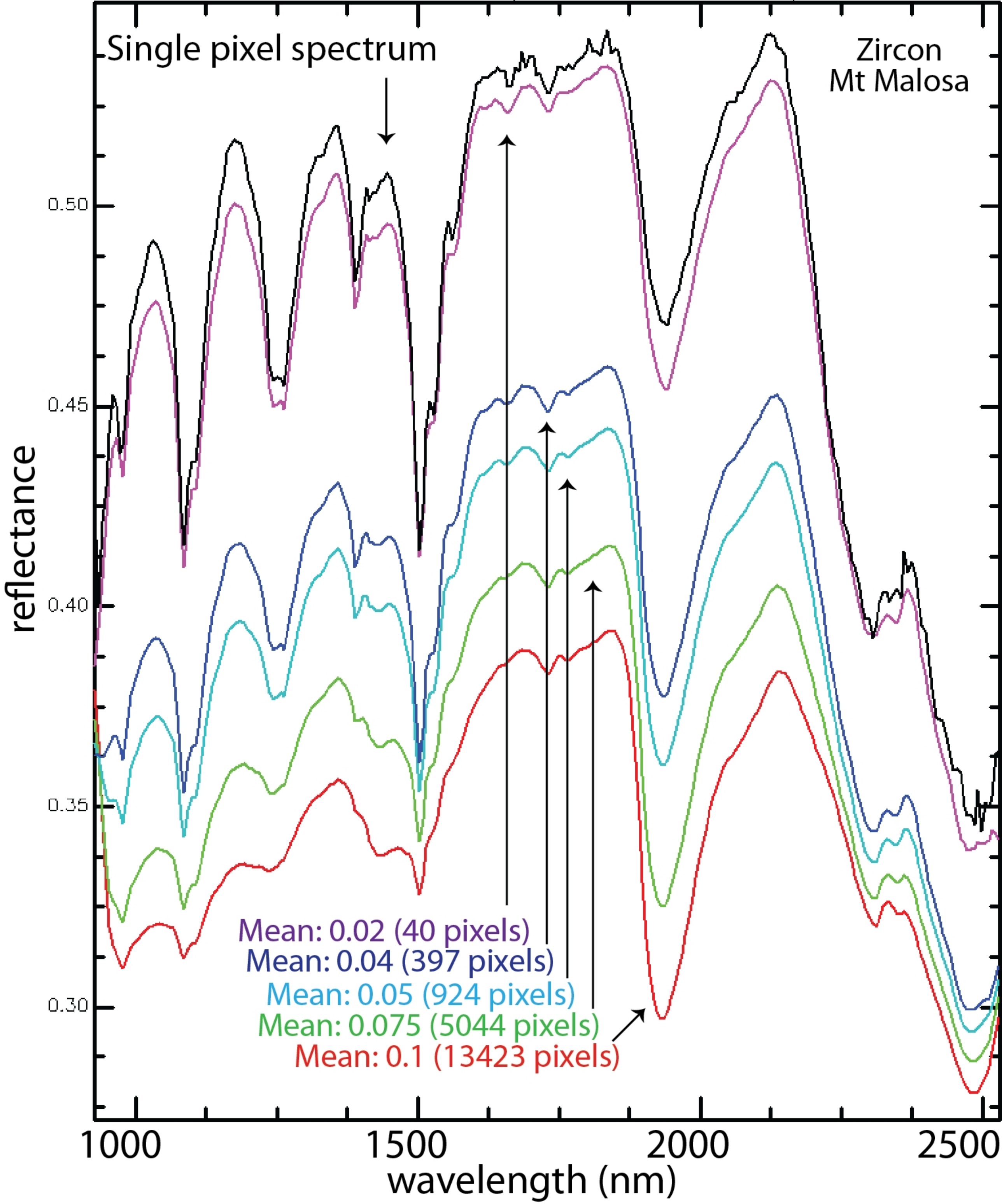
Single pixel spectrum
Zircon
Mt Malosa
reflectance
0.50
0.45
0.40
0.35
0.30
Mean: 0.02 (40 pixels)
Mean: 0.04 (397 pixels)
Mean: 0.05 (924 pixels)
Mean: 0.075 (5044 pixels)
Mean: 0.1 (13423 pixels)
1000
1500
2000
2500
wavelength (nm)

Figure 3

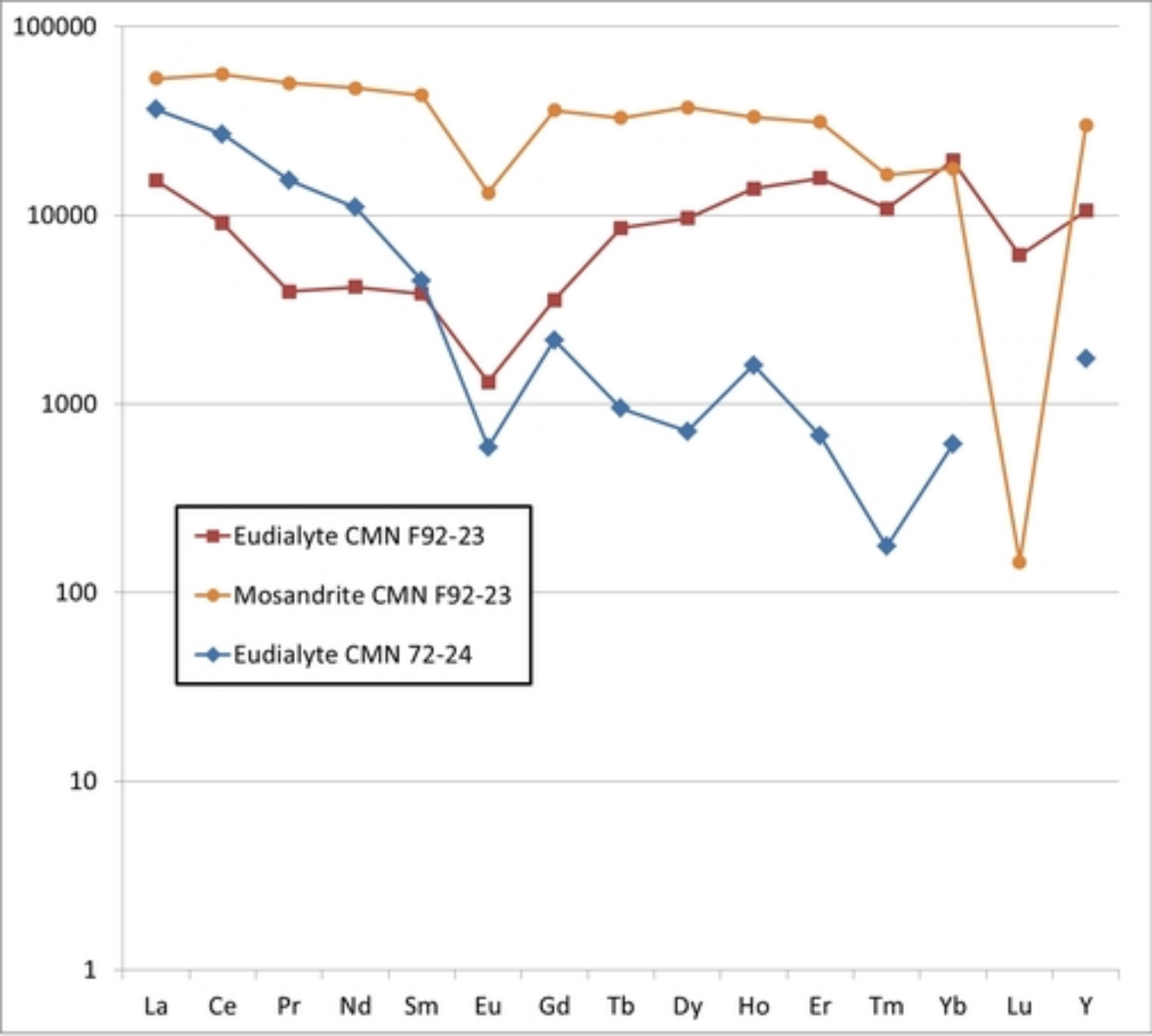
100000
10000
1000
100
10
1
Eudialyte CMN F92-23
Mosandrite CMN F92-23
Eudialyte CMN 72-24
La
Ce
Pr
Nd
Sm
Eu
Gd
Tb
Dy
Ho
Er
Tm
Yb
Lu
Y

Figure 4

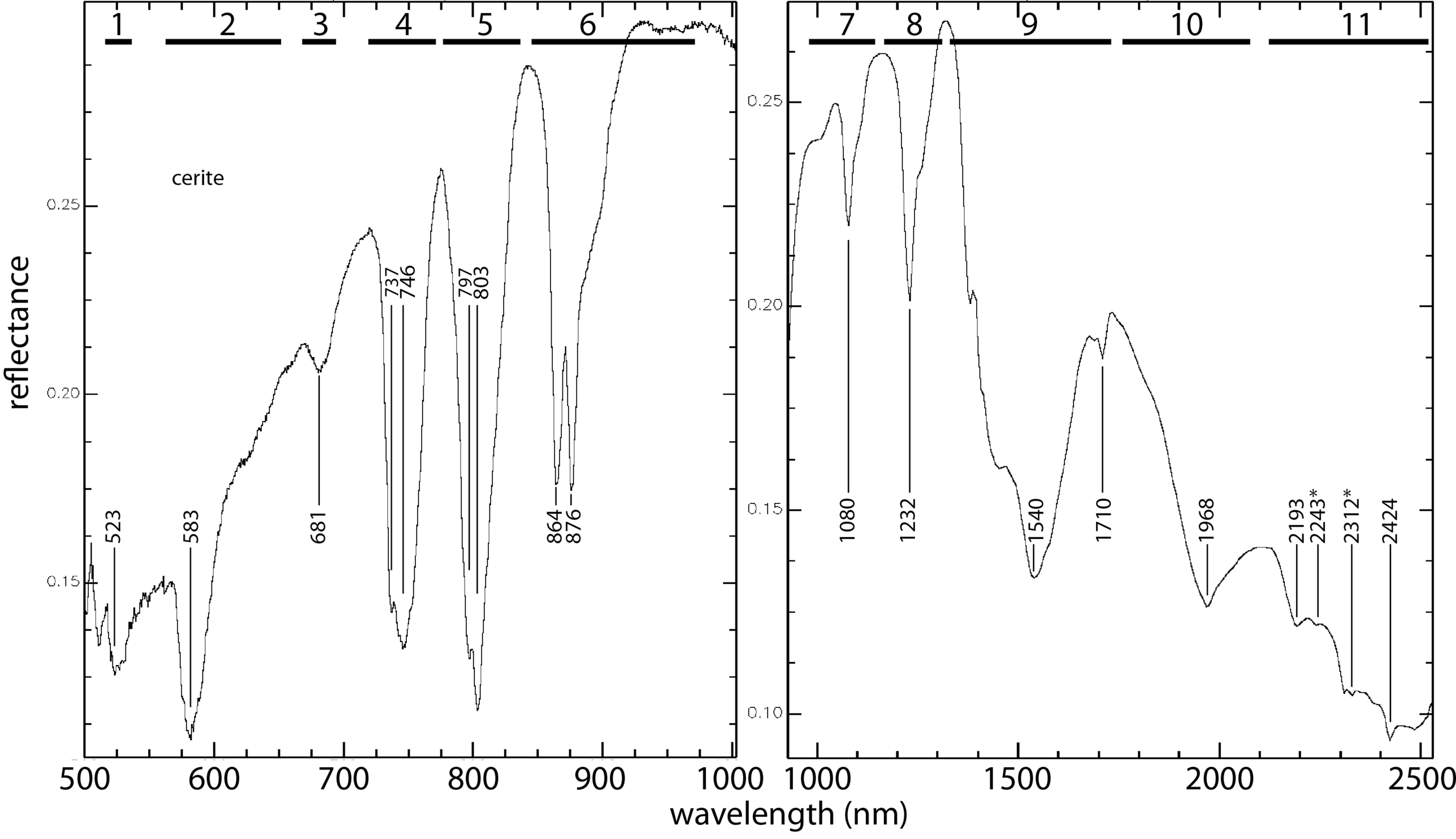
cerite
reflectance
wavelength (nm)
1
2
3
4
5
6
7
8
9
10
11
0.25
0.20
0.15
0.10
523
583
681
737
746
797
803
864
876
1080
1232
1540
1710
1968
2193
2243*
2312*
2424
500
600
700
800
900
1000
1000
1500
2000
2500

Figure 5

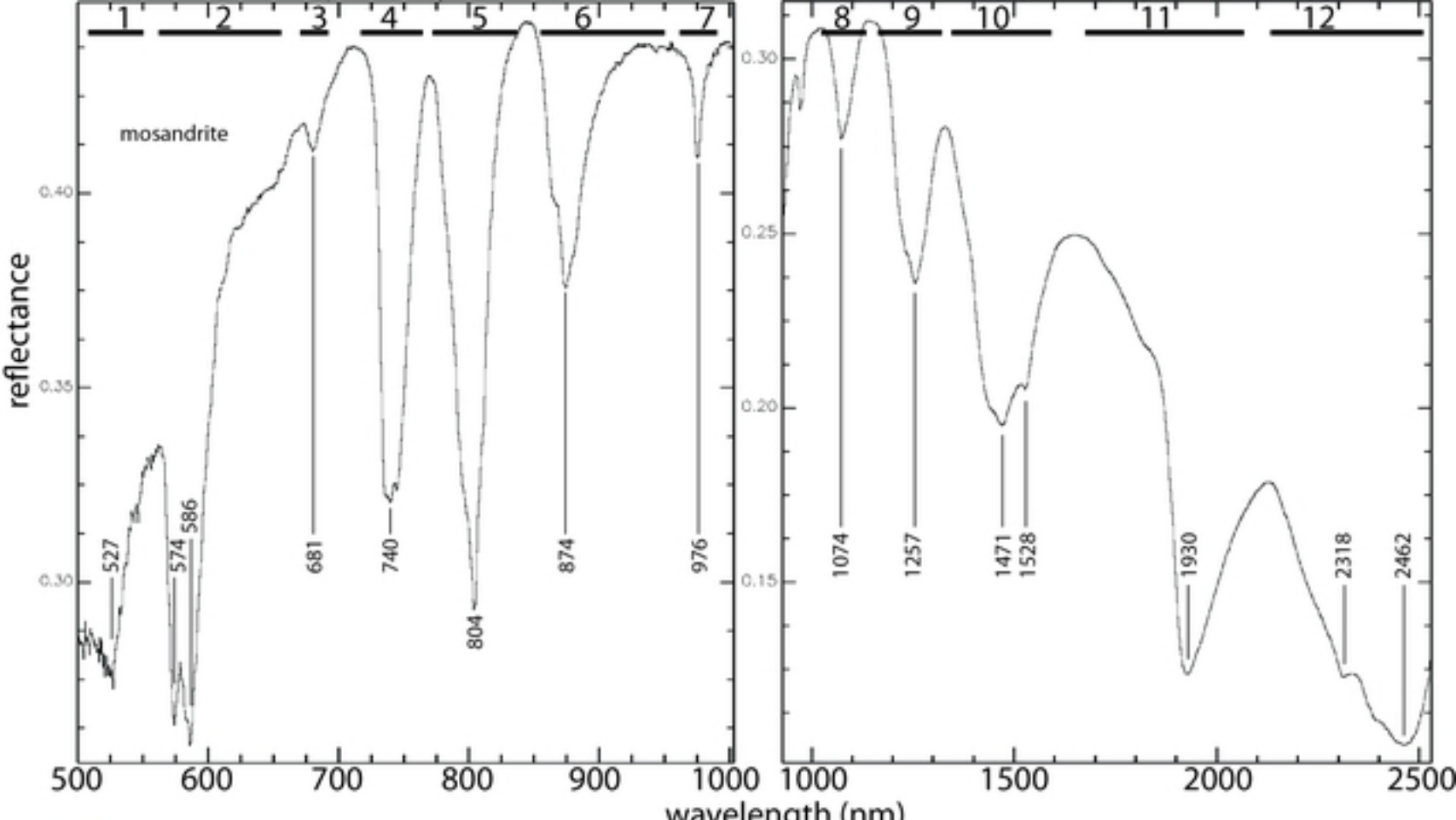
mosandrite
reflectance
wavelength (nm)
1
2
3
4
5
6
7
8
9
10
11
12
527
574
586
681
740
804
874
976
1074
1257
1471
1528
1930
2318
2462
0.40
0.35
0.30
0.25
0.20
0.15
500
600
700
800
900
1000
1500
2000
2500

Figure 6

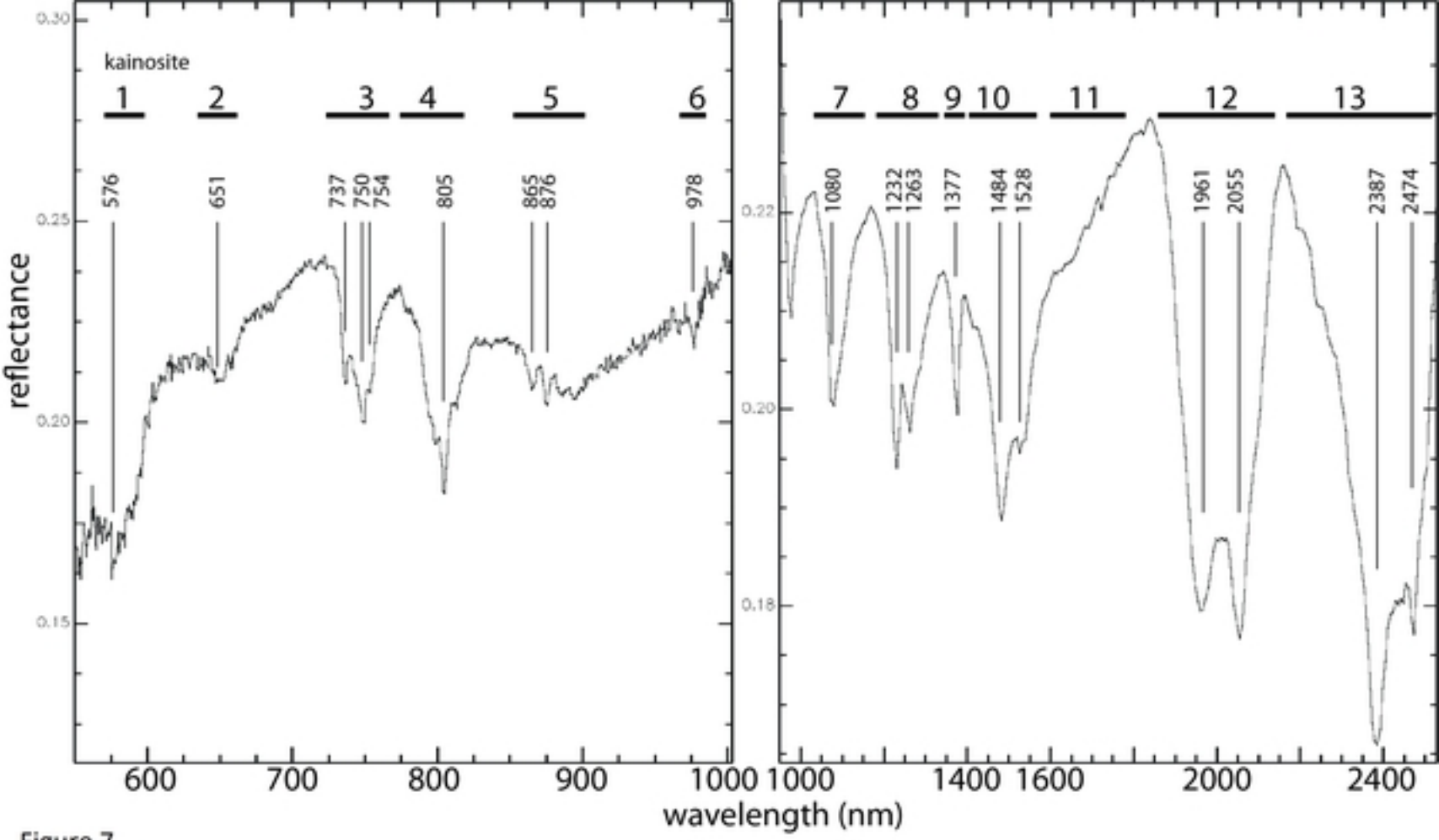
kainosite
1
2
3
4
5
6
7
8
9
10
11
12
13
576
651
737
750
754
805
865
876
978
1080
1232
1263
1377
1484
1528
1961
2055
2387
2474
reflectance
wavelength (nm)
0.30
0.25
0.20
0.15
0.22
0.18
600
700
800
900
1000
1400
1600
2000
2400

Figure 7

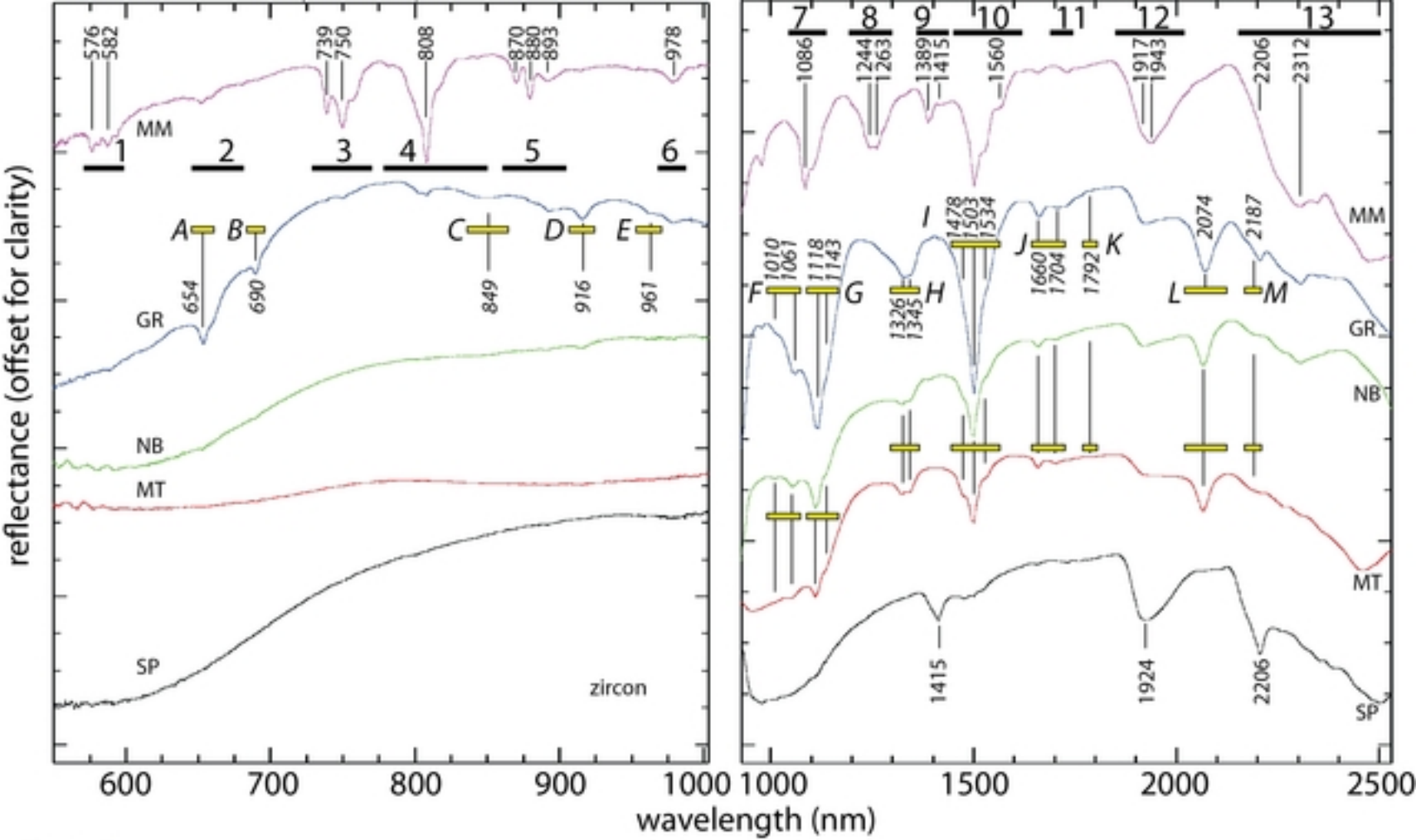
reflectance (offset for clarity)
wavelength (nm)
600
700
800
900
1000
1000
1500
2000
2500
MM
GR
NB
MT
SP
zircon
576
582
739
750
808
870
880
893
978
1086
1244
1263
1389
1415
1560
1917
1943
2206
2312
1
2
3
4
5
6
7
8
9
10
11
12
13
A
B
C
D
E
F
G
H
I
J
K
L
M
654
690
849
916
961
1010
1061
1118
1143
1326
1345
1478
1503
1534
1660
1704
1792
2074
2187
1415
1924
2206

Figure 8

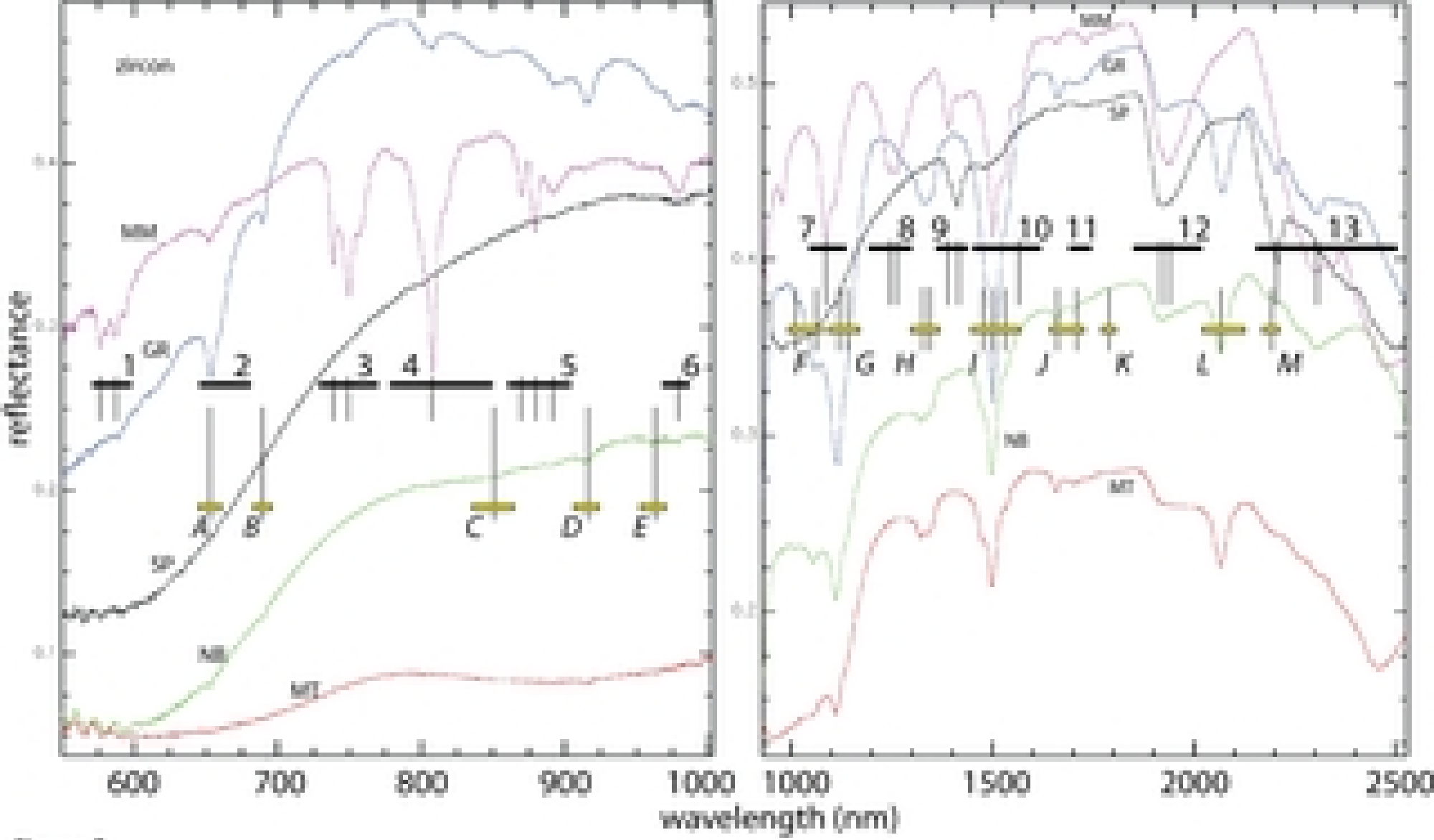
zircon
MM
GR
SP
NB
MT
1
2
3
4
5
6
A
B
C
D
E
7
8
9
10
11
12
13
F
G
H
I
J
K
L
M
reflectance
600
700
800
900
1000
1000
1500
2000
2500
wavelength (nm)

Figure 9

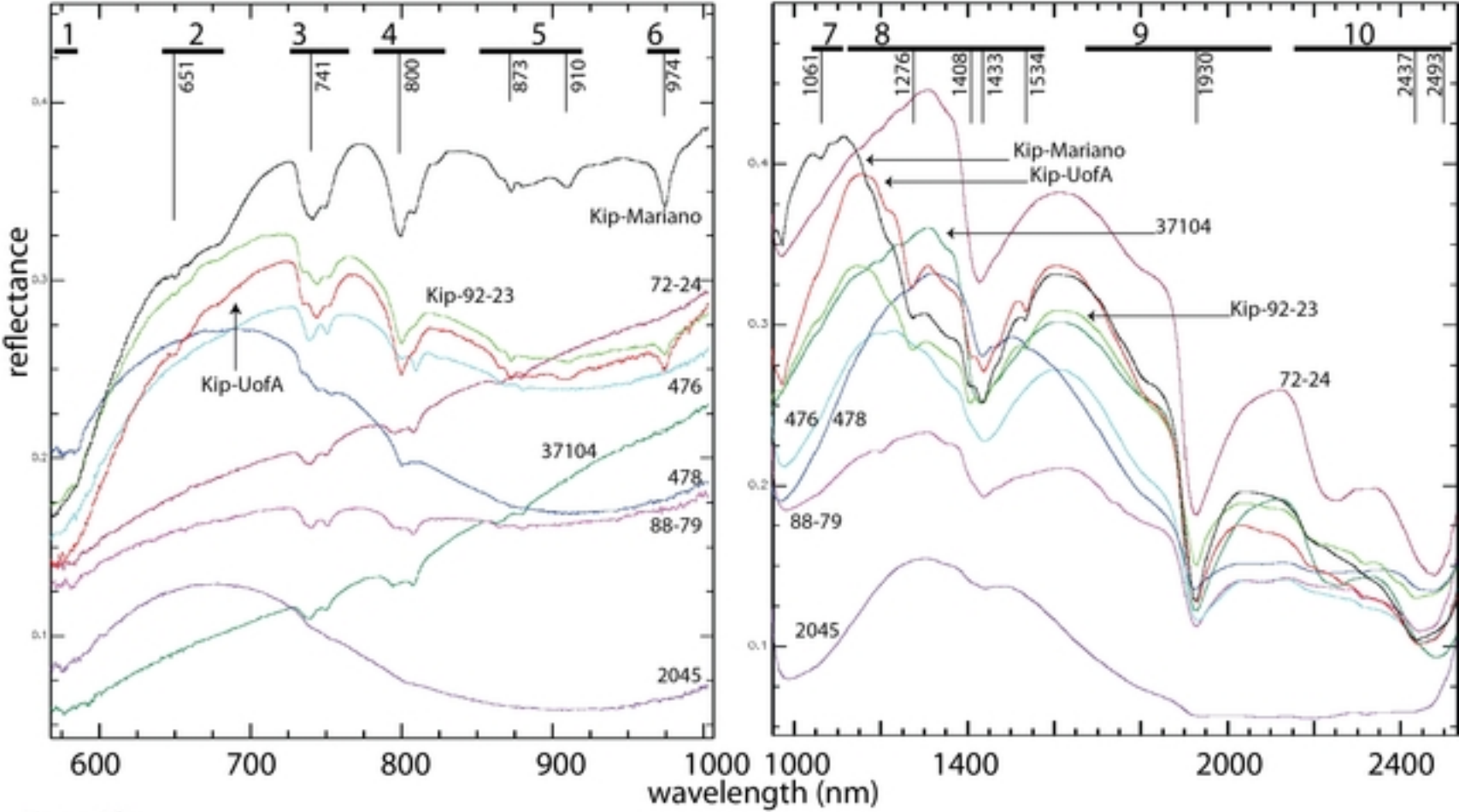
1
2
3
4
5
6
651
741
800
873
910
974
Kip-Mariano
Kip-92-23
Kip-UofA
72-24
476
37104
478
88-79
2045
reflectance
600
700
800
900
1000
7
8
9
10
1061
1276
1408
1433
1534
1930
2437
2493
Kip-Mariano
Kip-UofA
37104
Kip-92-23
72-24
476
478
88-79
2045
1000
1400
2000
2400
wavelength (nm)

Figure 10

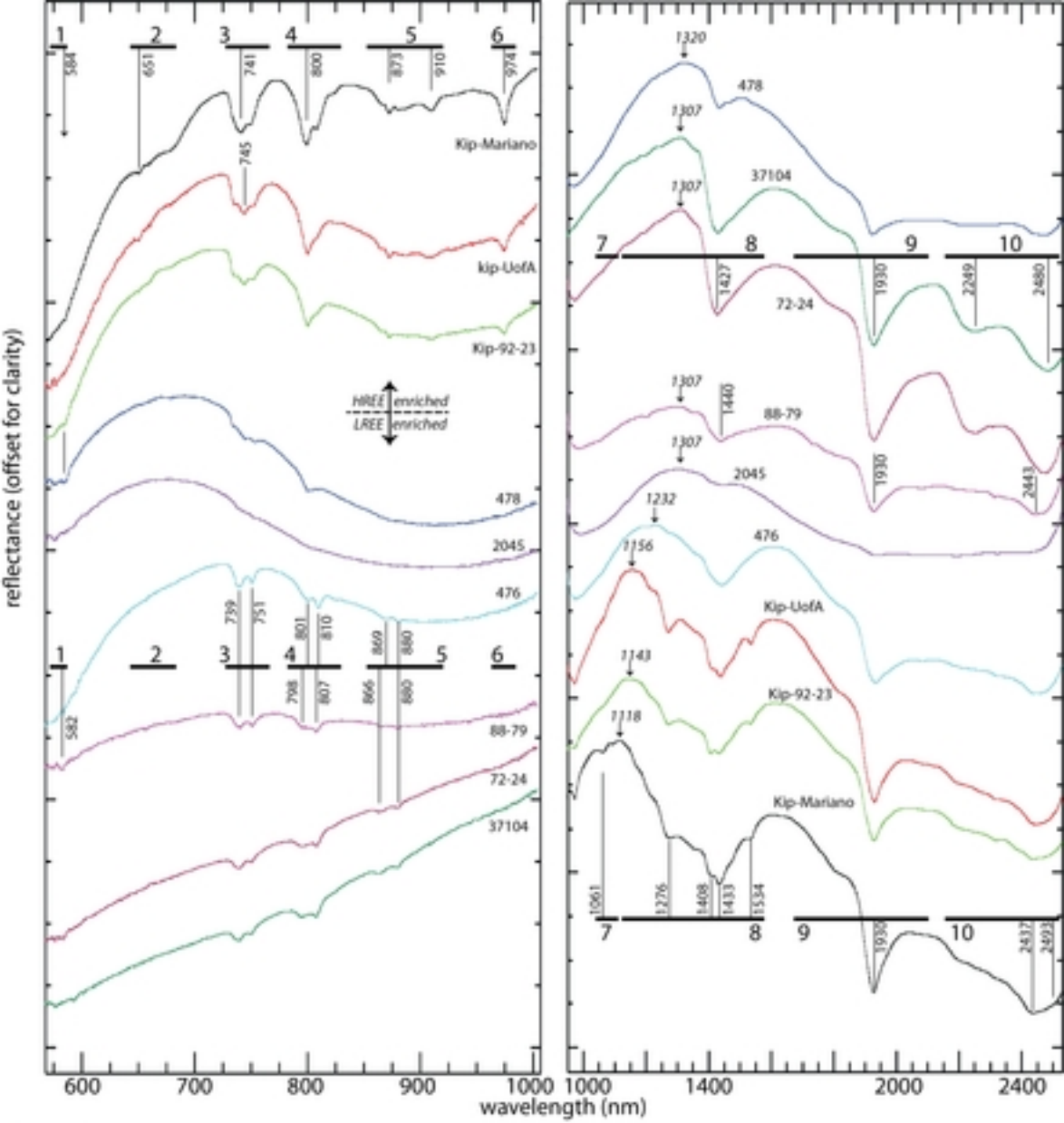
reflectance (offset for clarity)
wavelength (nm)
600
700
800
900
1000
1000
1400
2000
2400
1
2
3
4
5
6
584
651
741
800
873
910
974
745
Kip-Mariano
kip-UofA
Kip-92-23
HREE enriched
LREE enriched
478
2045
476
739
751
801
810
869
880
582
798
807
866
880
88-79
72-24
37104
1320
478
1307
37104
7
8
9
10
1427
1930
2249
2480
72-24
1307
1440
88-79
1307
1930
2045
2443
1232
476
1156
Kip-UofA
1143
Kip-92-23
1118
Kip-Mariano
1061
1276
1408
1433
1534
1930
2437
2493

Figure 11

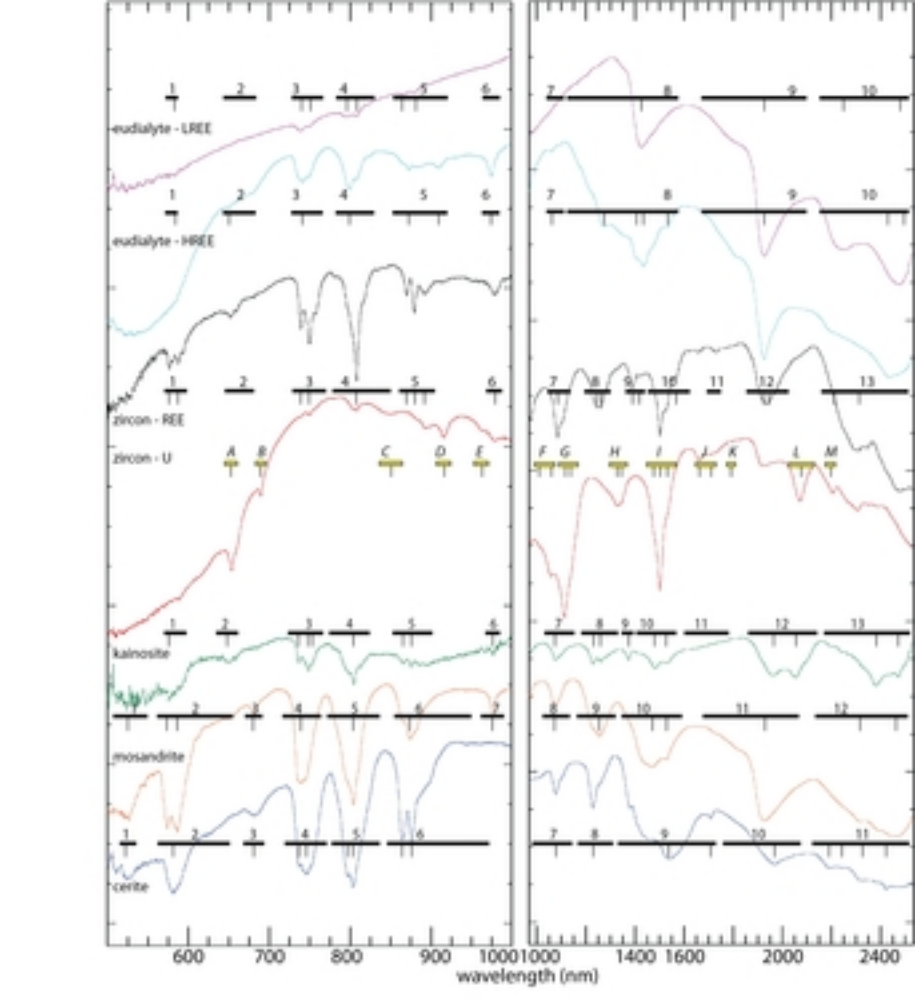
eudialyte - LREE
eudialyte - HREE
zircon - REE
zircon - U
kainosite
mosandrite
cerite
A B C D E F G H I J K L M
600 700 800 900 1000 1000 1400 1600 2000 2400
wavelength (nm)

Figure 12

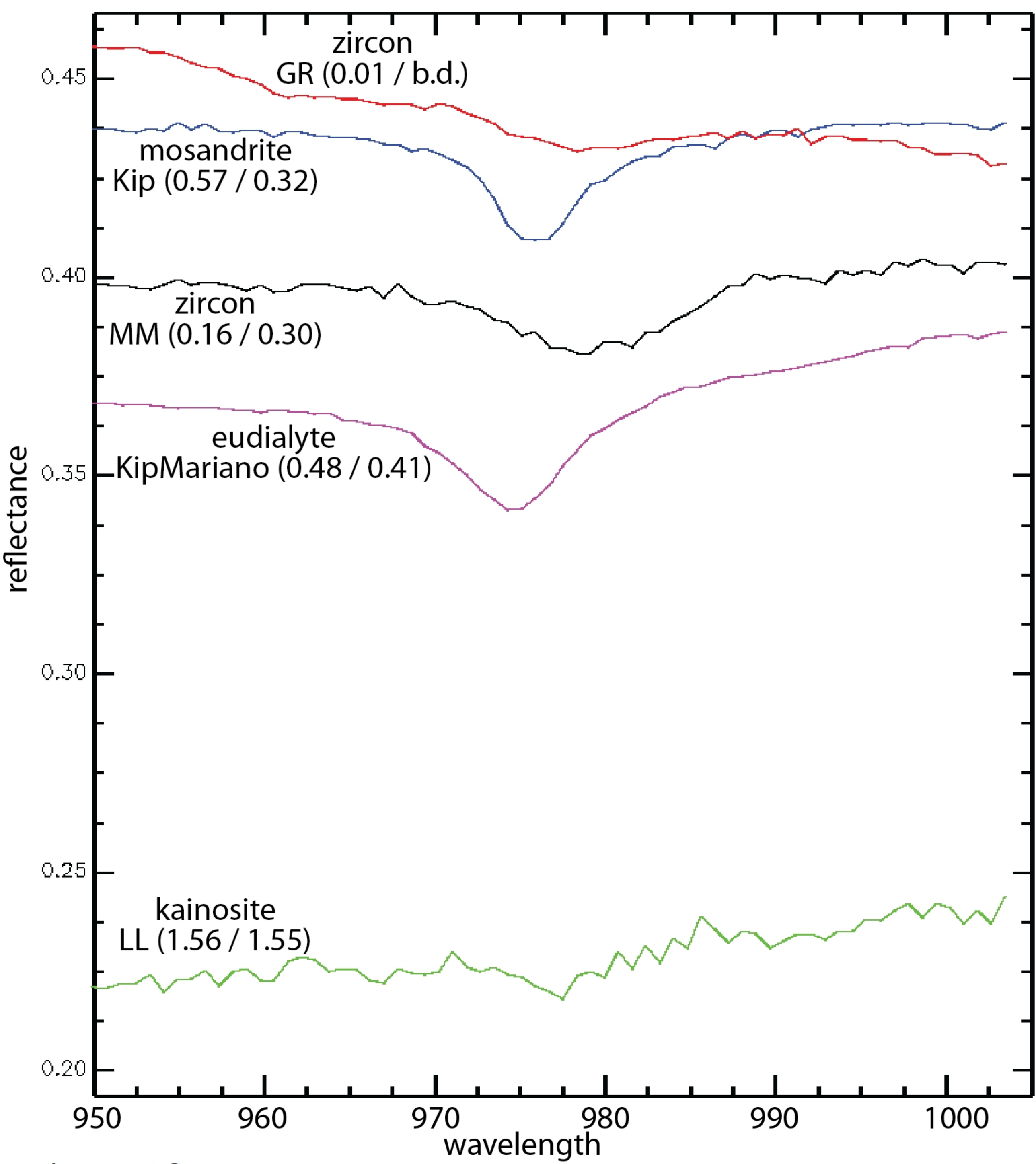
zircon
GR (0.01 / b.d.)
mosandrite
Kip (0.57 / 0.32)
zircon
MM (0.16 / 0.30)
eudialyte
KipMariano (0.48 / 0.41)
kainosite
LL (1.56 / 1.55)
reflectance
wavelength
0.45
0.40
0.35
0.30
0.25
0.20
950
960
970
980
990
1000

Figure 13

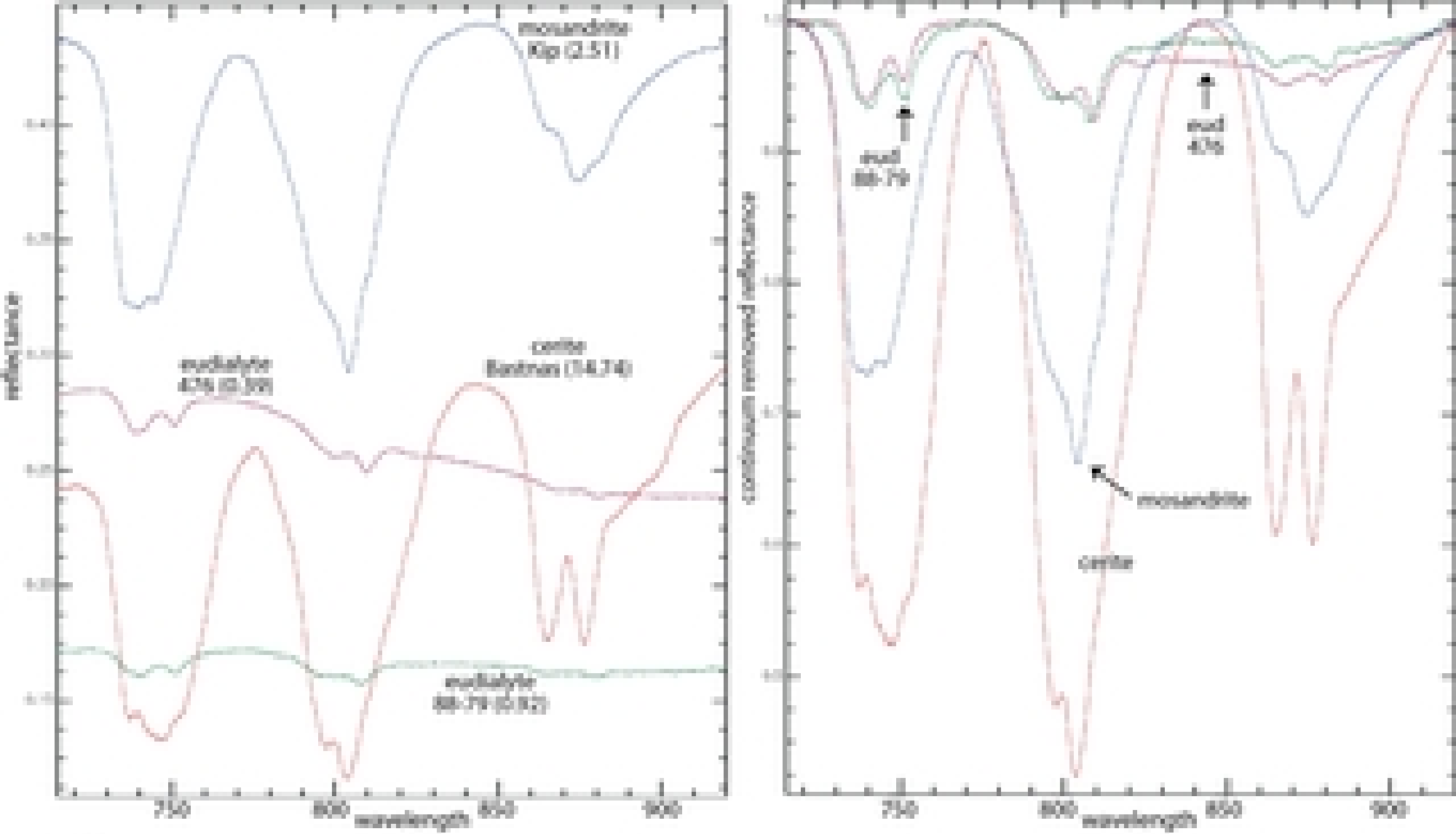
mosandrite
Klp (2.51)
eudialyte
476 (0.59)
cerite
Bastnas (14.74)
eudialyte
68-79 (0.92)
reflectance
wavelength
750
800
850
900
mud
68-79
mud
476
mosandrite
cerite
continuum removed reflectance
wavelength
750
800
850
900

Figure 14